Improved Madden–Julian Oscillations with Improved Physics: The Impact of Modified Convection Parameterizations

LEI ZHOU

Lamont-Doherty Earth Observatory, Columbia University, Palisades, New York, and Key Laboratory of Ocean Dynamic Processes and Satellite Oceanography, SOA, Hangzhou, China

RICHARD B. NEALE AND MARKUS JOCHUM

National Center for Atmospheric Research, Boulder, Colorado

RAGHU MURTUGUDDE

Earth System Science Interdisciplinary Center, University of Maryland, College Park, College Park, Maryland

ABSTRACT

Two modifications are made to the deep convection parameterization in the NCAR Community Climate System Model, version 3 (CCSM3): a dilute plume approximation and an implementation of the convective momentum transport (CMT). These changes lead to significant improvement in the simulated Madden–Julian oscillations (MJOs). With the dilute plume approximation, temperature and convective heating perturbations become more positively correlated. Consequently, more available potential energy is generated and the intraseasonal variability (ISV) becomes stronger. The organization of ISV is also improved, which is manifest in coherent structures between different MJO phases and an improved simulation of the eastward propagation of MJOs with a reasonable eastward speed. The improved propagation can be attributed to a better simulation of the low-level zonal winds due to the inclusion of CMT. The authors posit that the large-scale zonal winds are akin to a selective conveyor belt that facilitates the organization of ISVs into highly coherent structures, which are important features of observed MJOs. The conclusions are supported by two supplementary experiments, which include the dilute plume approximation and CMT separately.

1. Introduction

Madden–Julian oscillations (MJOs) are the dominant source of intraseasonal variability in the tropical atmosphere (Madden and Julian 1971, 1972, 1994, 2005). There have been numerous theories and model studies of MJOs to date, as summarized in Wang (2005) and Zhang (2005). Studies indicate that MJOs are closely related to phenomena occurring at different temporal and spatial scales, including the mean climate state (Inness et al. 2003; Sardeshmukh and Sura 2007), large-scale circulation, and small-scale convection (e.g., Blade and Hartmann 1993; Hu and Randall 1995; Kemball-Cook

and Weare 2001). Therefore, it would appear necessary to study MJOs keeping in mind that their life cycle occurs in a multiscale framework. Climate model simulations of MJOs still exhibit several substantial deficiencies. In particular, the eastward propagation of convection over the warm pool is not well simulated (Slingo et al. 1996), and the eastward phase speed is not consistent with observations (Waliser et al. 1999). A key factor in improving MJO simulation is the convective parameterization. Many tests have been conducted on the sensitivity of MJO simulation to various parameterizations (Wang and Schlesinger 1999; Maloney and Hartmann 2001a; Lin et al. 2008). Different convective parameterizations tend to differ in their ability to capture the intraseasonal variabilities (ISVs). Some studies (Chao and Deng 1998; Wang and Schlesinger 1999) indicate that the moist convective adjustment (MCA) (Manabe et al. 1965) scheme can generate the strongest ISVs, followed by Kuo scheme

Corresponding author address: Lei Zhou, 301d Oceanography, Lamont-Doherty Earth Observatory, 61 Route 9W, Palisades, NY 10964.
E-mail: lzhou@ldeo.columbia.edu

(Kuo 1974), with the modified Arakawa–Schubert scheme (Arakawa and Schubert 1974) generating the weakest ISVs.

Recently, the CLIVAR Madden–Julian Oscillation Working Group (2009) summarized the MJO diagnostics. The Level-2 diagnostics they proposed highlighted the organization (coherence) of MJOs between various variables and between different scales. They also emphasized that climate models have difficulty simulating this high degree of coherence. Therefore, it is reasonable to argue that the observed MJOs are not just enhanced ISVs but, more importantly, are also well-organized ISVs. Kim et al. (2009) analyzed eight model outputs following the standardized MJO diagnostics proposed in the CLIVAR Madden–Julian Oscillation Working Group (2009), hereafter the Working Group. They found that the ECHAM4/ Ocean Isopycnal Model (OPYC) displayed better skill in reproducing MJOs, which they argued was attributable to "a quite good mean state of precipitation and low-level wind."

In this study, the influence of two modifications to the convection scheme in the Community Climate System Model, version 3 (CCSM3) are tested. The magnitudes of ISVs produced by the original Zhang–McFarlane scheme (Zhang and McFarlane 1995) used in CCSM3 were much weaker than observations (Maloney and Hartmann 2001a; Maloney 2002). In addition, Maloney and Hartmann (2001a) showed that MJO simulations in CCSM3 are highly sensitive to the evaporation of convective precipitation in unsaturated environmental air and saturated downdrafts. They also showed that the simulated wind anomalies, which were weaker than reality, were unfavorable for MJO simulation. Possible improvement to MJO simulation due to an improvement in mean state has been studied with model experiments (Inness and Slingo 2003; Inness et al. 2003; Sperber et al. 2005; Ray et al. 2011), observations (Zhang and Dong 2004; Maloney and Hartmann 2001b), and model–observation comparisons (Zhang et al. 2006). Including the convective momentum transport (CMT) in a model may improve the simulation of large-scale winds since CMT represents the feedback of unresolved properties to the background state. Biello and Majda (2005) established a multiscale model that resolved both upscale and downscale energy transfer associated with MJOs. Majda and Stechmann (2009) assumed explicit forms of perturbations to the mean state and resolved CMT, which is critical for the interactions between the mesoscale and planetary scale, in a simple dynamical model and reproduced major features of MJOs on multiple scales. Since all perturbations bear an explicit form, no parameterization is necessary. Hence, their analytical method is quite different from the parameterization of CMT in our model experiments, which will be introduced below. Another reason for poor MJO simulation is believed to be too frequent deep convection generated by models. Both theoretical work and observations indicate that eastward propagation of MJOs is related to the reduced shallow convective heating (Lau and Peng 1987; Sui and Lau 1989; Webster and Lukas 1992), which moistens the lower troposphere (Zhu et al. 2009) and suppresses deep convection before the active phase of MJOs (Johnson et al. 1999; Tian et al. 2006, 2010). Since a dilute plume approximation (DPA) may inhibit some deep convection, it can be expected to help improve MJO simulation.

Generally, two aspects of convective parameterization that have long been thought deficient in MJO simulation are the lack of explicit linkage to subgrid-scale momentum transfer and the insensitivity to free-tropospheric (above boundary layer) humidity. Observational evidence demonstrating the potential importance of these linkages and motivating their inclusion in parameterization schemes come from a wide range of observed convective phenomena and not just the MJO. For example, moisture sensitivity is believed to be key in capturing the correct phase of the diurnal cycle of rainfall over land as successively deeper entraining clouds premoisten a deep level of the atmosphere and delay the peak in rainfall and convection to generally occur in the late afternoon or early evening (e.g., Chaboureau et al. 2004). Parameterization schemes in coarse grid GCMs are unable to represent this slow diurnal humidity evolution and, instead, the response is too strongly tied to surface temperature which peaks much earlier in the day (e.g., Bechtold et al. 2004). Coarse grid GCMs also do not resolve mesoscale transports of momentum inherent to convectively coupled propagating systems such as squall lines, U.S. summertime systems, and equatorial wave propagation in general. The MJO should benefit from increased sensitivity to tropospheric moisture, given the observed occurrence of progressive premoistening ahead of each event's convecting maximum (e.g., Benedict and Randall 2007; Lin et al. 2008) and the simulation of a moisture mode setting an MJO strength, speed, and time scale (e.g., Sugiyama 2009). In addition, the multiscale nature of the MJO envelope is thought to contain significant upscale momentum transport and may benefit from the representation of subgrid momentum transports (e.g., Sperber and Waliser 2008). In Kim et al. (2009), MJO simulations in eight models are compared. The model features concerning DPA and CMT are listed in Table 1 (D. Kim 2011, personal communication). The model producing the best MJOs is ECHAM4, which adopts both DPA and CMT. Therefore, in this study, two modifications are made to the convection scheme in CCSM3—implementing DPA and CMT. As a result, the simulated MJOs become more

TABLE 1. Features of the models used in Kim et al. (2009). Models not in text are Climate Forecast System (CFS), Climate Model version 2.1 (CM2.1), Geophysical Fluid Dynamics Laboratory (GFDL), Goddard Earth Observing System Model, version 5 (GEOS5), Super-Parameterization CAM (SPCAM), Scripps Institution of Oceanography (SIO), Seoul National University (SNU), and Colorado State University (CSU).

Models in Kim et al. (2009)	CMT	DPA
CAM3.5-NCAR	Yes	Yes
CAM3z-SIO	No	No
CFS*-NCEP	Yes	No
CM2.1*-GFDL	Yes	No
ECHAM4/OPYC*-MPI	Yes	Yes
GEOS5-NASA	No	No
SNU-SNU	No	No
SPCAM-CSU	No	Not applicable

* A model name with an asterisk denotes a coupled model (D. Kim 2011, personal communication).

energetic and the ISVs have more coherent structures with enhanced realism compared to observed MJO events. In section 2, CCSM3 model configurations are described and differences in background states in the two model runs are highlighted. The improvements in the strength and the coherence of simulated MJOs are analyzed in sections 3 and 4, respectively. The increase in the MJO strength is moderate, while the improvement in the organization of the simulated MJOs is profound. Thus, the latter part is the prime focus of this study. Conclusions and discussion are presented in section 5.

2. Model description

CCSM3 is a state-of-the-art, global climate model that fully couples the atmosphere, ocean, land, and sea ice (Collins et al. 2006a,b). The perturbed deep convection model configurations are described in detail in Neale et al. (2008). Hence, only the relevant aspects are briefly mentioned here. The atmospheric component is based on the Community Atmosphere Model, version 3 (CAM3) (Collins et al. 2006a), with 26 vertical levels and a horizontal resolution of 1.9° latitude × 2.5° longitude. There are 40 vertical levels in the ocean component with a nominal horizontal resolution of 1° × 1°. The parameterization of the deep convection basically follows the Zhang and McFarlane (1995) scheme, but with two modifications. One is DPA (Raymond and Blyth 1986, 1992), in which mixing occurs at all levels (not only at the cloud top) between the lowest model level and the neutral buoyancy level for a rising air parcel. According to DPA, air parcels seek their neutral buoyancy level and their specific entropy is conserved during the vertical motion. Mixing between the reference parcel and the free troposphere is dependent on an assumed entrainment rate. The other one is the inclusion of CMT following Kershaw and Gregory

(1997), which represents the compensation of convective momentum transport by atmospheric subsidence. The CMT parameterization follows the mass-flux approach and decomposes the product $\overline{u'w'}$, where u' and w' are unresolved perturbations to the zonal and vertical velocities, into three components: updraft, downdraft, and environment [see Eq. (3) in Kershaw and Gregory (1997) for technical details]. More details about these two modifications can be also found in Neale et al. (2008). Two fully coupled CCSM experiments were performed: one is the control run (referred to as C3OLD hereafter) without the above two changes and the other one includes the two modifications (referred to as C3NEW hereafter). Both experiments are conducted for 102 years, and the last 20 years (Year 83–Year 102) provide the period of focus for the daily output analysis. A caveat for daily outputs is that the diurnal cycle in the surface heat flux and precipitation is significant over the Maritime Continent, as discussed in Sobel et al. (2008, 2010). Nevertheless, so as to test the impacts of these two modifications on the MJO simulation, daily outputs are still the most suitable for our stated purpose. In the following, we will show that the two modifications to the Zhang–McFarlane scheme contribute in different ways to the improved MJO simulations. To further understand the separate roles of the convective parameterization changes, two supplementary runs are performed: one including the DPA only (referred to as C3DPA hereafter) and one including CMT only (referred to as C3CMT hereafter). Both supplementary runs are conducted for 50 years, and the last 10 years (year 41–year 50) with daily outputs are used for analysis.

With the inclusion of CMT, the easterly bias of low-level zonal winds in the tropics is reduced, which has been reported in detail by Richter and Rasch (2008) and Neale et al. (2008). The zonal momentum budget can be written as

$$\frac{\partial u}{\partial t} + \left(u\frac{\partial u}{\partial x} + v\frac{\partial u}{\partial y} + w\frac{\partial u}{\partial p} \right) - fv = \frac{\partial \varphi}{\partial x} + X, \quad (1)$$

where u and v are zonal and meridional velocities, w is the vertical pressure velocity, f is the Coriolis parameter, φ is the geopotential, and X is a residual term that mainly contains CMT (Tung and Yanai 2002). All terms at 850 hPa for the last year (averaged within 10°N–10°S, 80°–100°E) are shown in Fig. 1. With our CCSM3 model outputs, the results indicate that $\partial\varphi/\partial x$ and X are two dominant terms, which is consistent with previous findings (e.g., Lin et al. 2005; Ray and Zhang 2010). The correlations between $\partial u/\partial t$ and all other terms in the zonal momentum budget [Eq. (1)] are listed in Table 2. All components are at 850 hPa and averaged within 10°N–10°S, 80°–100°E. The correlations between $\partial\varphi/\partial x$ and $\partial u/\partial t$ are insignificant in all model experiments (regular numbers in Table 2), indicating that, although $\partial\varphi/\partial x$ is
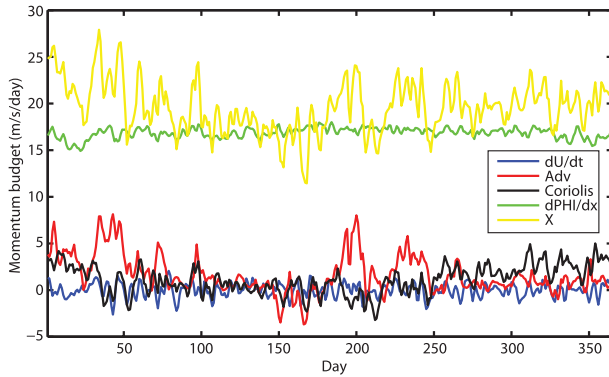
FIG. 1. Components in the zonal momentum budget [Eq. (1)] for the last year in C3NEW. All terms are calculated at 850 hPa and averaged within 10°N–10°S, 80°–100°E: "Adv" represents $u\partial u/\partial x + v\partial u/\partial y + w\partial u/\partial p$ and "Coriolis" represents $-fv$.

a large term in the zonal momentum budget (Fig. 1), it plays a minor role in determining the zonal momentum tendency. In contrast, the correlations between X and $\partial u/\partial t$ are always statistically significant (bold numbers in Table 2), indicating that CMT is intimately related to the zonal wind tendency. Especially for the model experiments adopting the CMT parameterization (i.e., C3NEW and C3CMT), the correlations between $\partial u/\partial t$ and X increase, which implies a fairly strong influence of CMT on the zonal wind tendency. Note that the correlations in Table 2 are calculated with the 20-yr outputs and not with the only 1-yr outputs shown in Fig. 1. The positive correlations between $\partial u/\partial t$ and X are not contrary to the previous conclusion in Lin et al. (2005), which concluded that CMT contributes negatively to the zonal wind tendency. Lin et al. (2005) discussed the zonal momentum budget for MJOs. Thus, they focused on "the zonal momentum equation for intraseasonal anomalies of deviations from the zonal mean." In contrast, we calculate the total zonal momentum budget, Eq. (1), and no filtering is applied to any variables. The positive correlations between $\partial u/\partial t$ and X in the lower level from the Indian Ocean to the western Pacific Ocean can be also obtained with the National Centers for Environmental Prediction (NCEP) reanalysis (not shown). Therefore, the relations between X and $\partial u/\partial t$ in Lin et al. (2005) and in the current study are on different scales and are not comparable.

The improvement in the mean westerly winds can be seen in Fig. 2. Generally, the mean zonal winds at 850 hPa are quite similar in the two model runs (Figs. 2c and 2e). However, pronounced westerly winds from the central tropical Indian Ocean to the Maritime Continent (approximately from 50° to 150°E, Fig. 2c) are reproduced, although they are a little stronger than the NCEP reanalysis (Kalnay et al. 1996; Fig. 2a) over the Maritime Continent (Fig. 2d). The climatological winds in C3CMT (Fig. 2h) are

TABLE 2. Correlations between the zonal momentum tendency ($\partial u/\partial t$) and all other terms in the zonal momentum budget, Eq. (1). Daily outputs for 20 years are used for C3OLD and C3NEW, while daily outputs for 10 years are used for C3CMT and C3DPA. "Advection" represents $u\partial u/\partial x + v\partial u/\partial y + w\partial u/\partial p$, "Coriolis" represents $-fv$. The bold numbers are correlations statistically significant at a confidence level of 95%. All components are at 850 hPa and averaged within 10°N–10°S, 80°–100°E.

| | Correlations between $\partial u/\partial t$ and | | | |
	Advection	Coriolis	$\partial\varphi/\partial x$	X
$\partial u/\partial t$ C3OLD	**−0.1607**	**0.0924**	0.0233	**0.2605**
$\partial u/\partial t$ C3NEW	−0.0223	**0.1821**	0.0206	**0.3645**
$\partial u/\partial t$ C3CMT	**−0.0707**	**0.0692**	0.0009	**0.3702**
$\partial u/\partial t$ C3DPA	**−0.0870**	**0.2287**	0.0305	**0.2234**

very similar to those in C3NEW (Fig. 2c), which again demonstrates the influence of CMT on improving the low-level zonal winds. In contrast, the westerly winds can barely be found in the warm-pool region in C3OLD (Figs. 2e and 2f). Zonal winds at 850 hPa in C3DPA (Fig. 2g) also have the easterly wind bias over this region, which is similar to the situation in C3OLD (Fig. 2e).

Besides the background zonal winds, other background fields are also modified to various degrees due to the two modifications in the convection scheme. Figure 3 shows the differences between the mean state in C3NEW and C3OLD normalized by the standard deviation (STD) in C3NEW. These ratios are similar to the standard error used in Agudelo et al. (2009). The differences in low-level zonal winds (Fig. 3a) between C3OLD and C3NEW are comparable with the STDs in C3NEW from the tropical Indian Ocean to the western Pacific Ocean, which is also the major region with improved westerly winds. The differences in the air temperature at 850 hPa (Fig. 3b) between the two model runs are comparable with their STD in C3NEW over the southwestern Indian Ocean and the western Pacific Ocean. But, over the Maritime Continent, the differences in temperature are not very large. Actually, the large differences in the air temperature are partly due to the increased energy imbalance in C3NEW. The energy imbalance over 102 years in C3OLD is 0.3 W m^{-2} compared to 0.7 W m^{-2} in C3NEW. Therefore the coupled system in C3NEW adds heat at more than twice the rate of C3OLD. So it is inevitable that there will be a nonnegligible climate divergence during the last 20 years, which is the center of our analysis. Surface temperature bias is thus not the best indicator of convection change effects, but the simulation differences are robust as they are also seen in uncoupled, prescribed sea surface temperature experiments. For zonal winds, the comparison is more suitable because the SST gradient ($\partial SST/\partial x$ and $\partial SST/\partial y$) is less affected by trend. For the latent heat flux (Fig. 3c), which can play a critical role in tropical ISVs

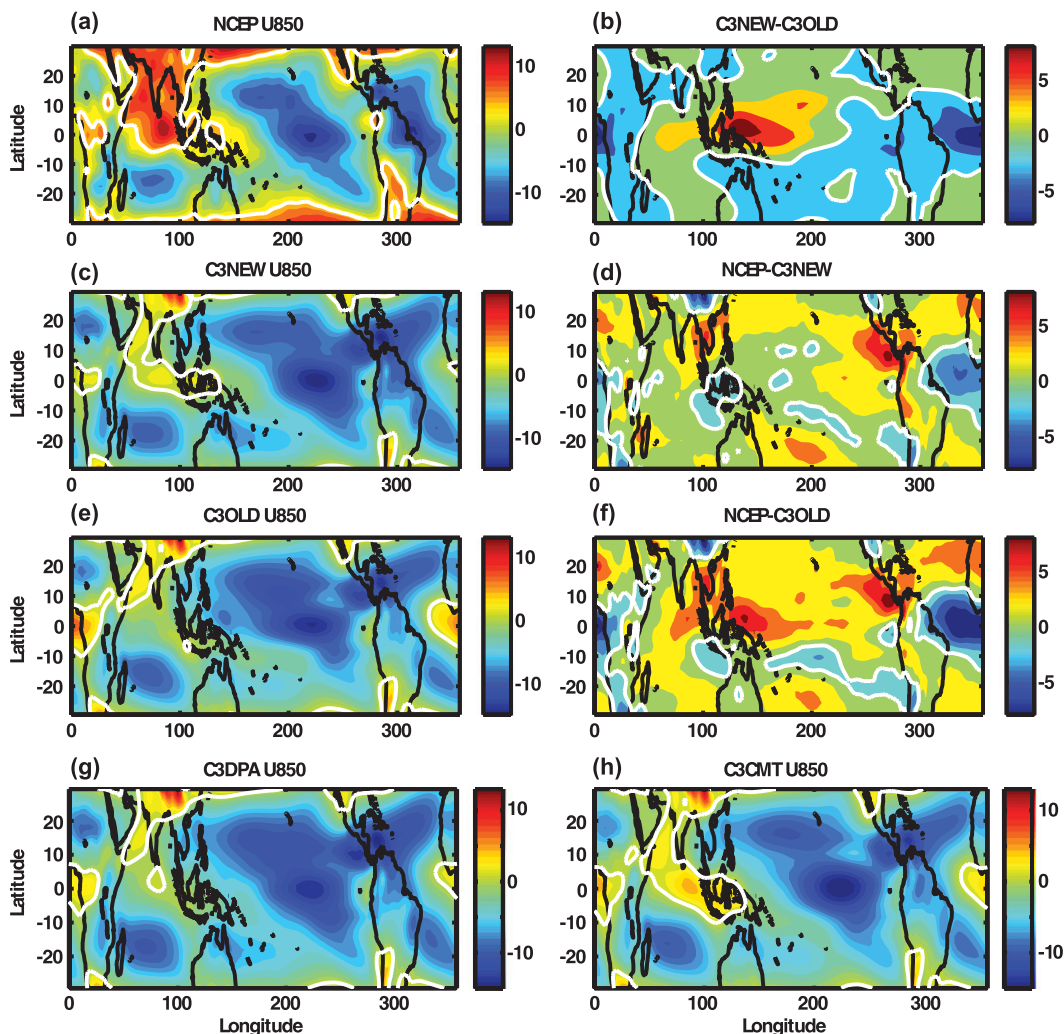FIG. 2. Mean zonal winds (m s^{-1}) at 850 hPa in the (a) NCEP reanalysis from 1979 to 2009, (c) C3NEW, (e) C3OLD, (g) C3DPA, and (h) C3CMT. Differences between (b) C3NEW and C3OLD, (d) NCEP and C3NEW, and (f) NCEP and C3OLD are shown. White contours correspond to zero.

(e.g., Sobel et al. 2008, 2010), the differences between the two model runs are much smaller than their variations in C3NEW. In addition, the vertically averaged (from 1000 to 200 hPa) moist static energy (MSE) ($h = C_pT + Lq + gz$, where C_p is the specific heat of the air, T the air temperature, q the specific humidity, g the gravitational acceleration, and z the geopotential height) is calculated. The differences in MSE between the two model runs are shown in Fig. 3d. Probably owing to the influence of temperature, the normalized differences over the southwestern Indian Ocean can be as large as 0.6. But in the deep tropics from the Indian Ocean to the western Pacific Ocean, the differences are always very small. Since MSE is a good indicator of the stability of the air column (Kemball-Cook and Weare 2001), the similarity between the two model runs indicates that the stabilities of the

background state have no notable differences between C3NEW and C3OLD in the deep tropics. Note however that these stabilities are reached after adjustments in the coupled systems and the state variables such as winds and precipitation do display differences in spatial and temporal scales. In all, the two modifications in the convection parameterization result in variations in all variables. Nevertheless, the variation in low-level winds is the most significant one. In section 4, we will show that a better organization of simulated MJOs in C3NEW is closely related to the improved background westerly winds.

3. Strength of the intraseasonal variabilities

By examining the variance of the intraseasonal zonal winds at 200 hPa (Slingo et al. 1999) over the tropical
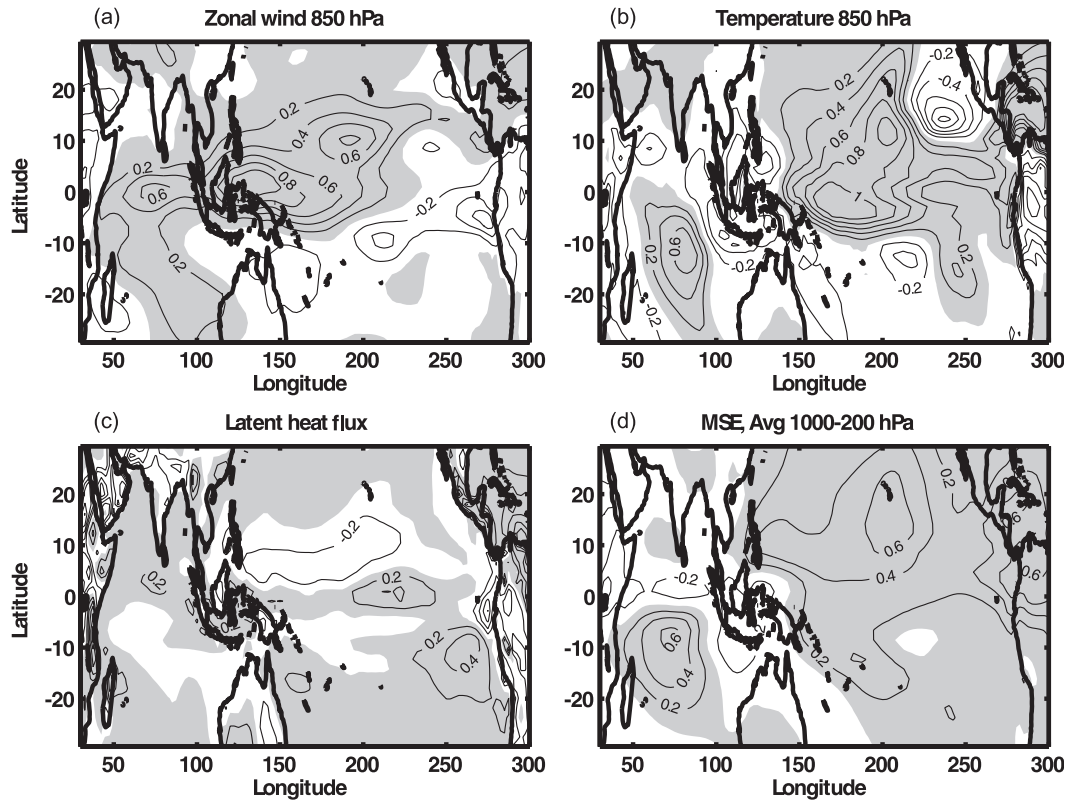
FIG. 3. Differences of (a) zonal winds at 850 hPa, (b) air temperature, (c) latent heat flux, and (d) vertically averaged MSE, normalized by the corresponding STDs in C3NEW. All ratios are dimensionless; positive ratios are shaded.

Indian Ocean, Zhang and Mu (2005, their Fig. 3) showed that applying a modified Zhang–McFarlane scheme for deep convection could considerably increase the strength of ISVs in CCSM3. With the same method, one can see energetic ISVs in C3OLD (using the Zhang–McFarlane scheme with no modifications), which reaffirms that adopting Zhang–McFarlane scheme can indeed produce strong ISVs in a model (not shown). Nevertheless, a more targeted MJO index [created with zonal winds at 200 and 850 hPa and outgoing longwave radiation (OLR; Wheeler and Hendon 2004)] is used in this study. The variance time series of $(PC1^2 + PC2^2)^{1/2}$ after a 91-day running mean is shown in Fig. 4, where PC1 and PC2 are the principal components of the first two EOF modes of the multivariate field (see Wheeler and Hendon for details). Daily MJO index during specified MJO events is shown below in the phase diagram. The ISVs in C3NEW are in general stronger than those in C3OLD, for example, in years 87, 88, 90, and 96. The stronger ISVs in C3NEW can also be clearly seen in the individual variables, such as the intraseasonal zonal winds at 850 hPa and OLR (Neale et al. 2008). For example, the mean STD of the intraseasonal zonal winds at 850 hPa averaged within the zonal belt region

between 15°N and 15°S is 2.1 m s^{-1} for C3NEW and 1.7 m s^{-1} for C3OLD. For the intraseasonal zonal winds at 200 hPa, such mean STD is 4.4 m s^{-1} for C3NEW and 4.0 m s^{-1} for C3OLD, respectively. For the intraseasonal OLR anomalies, the mean STD computed similarly is 18.3 W m^{-2} for C3NEW and 16.2 W m^{-2} for C3OLD. Note that the impacts of model differences in monsoons, ENSO, and their interactions on the ISVs are beyond the scope of this work and are not considered here. The MJO index in C3CMT and C3DPA look similar in Fig. 4 but, actually taking an average over 10 years, the index is a little larger in C3DPA than in C3CMT. At 850 hPa the STDs of the intraseasonal zonal winds in C3NEW (Fig. 5c) are similar to those in the NCEP reanalysis (Fig. 5a). Generally, the differences between C3NEW and NCEP are smaller than 0.5 m s^{-1} over the tropical Indian Ocean and the western Pacific Ocean (Fig. 5b). However in C3OLD, the ISVs in this region are not distinctly different from other tropical regions (such as the central Pacific Ocean and the Atlantic Ocean, Fig. 5e). As clearly shown in Figs. 5d and 5f, the major enhancement in the intraseasonal zonal winds in C3NEW is over the Indo-Pacific warm pool. Therefore, with the modifications to the deep convection parameterization (Neale et al. 2008), the
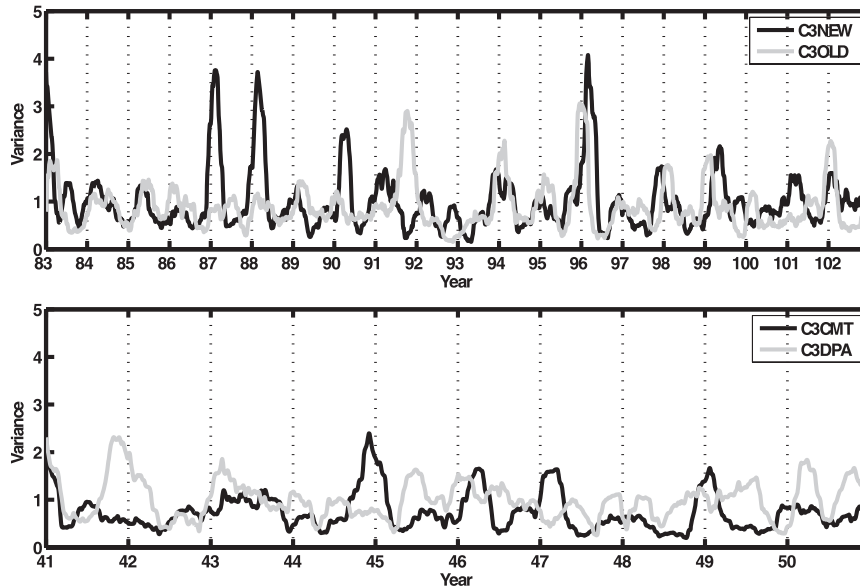
FIG. 4. MJO index created with simulated zonal winds at 850 and 200 hPa and OLR, following
Wheeler and Hendon (2004).

tropical ISVs in C3NEW become generally more energetic than those in C3OLD.

Mean precipitation in C3NEW and C3OLD is compared in Fig. 6. The general patterns in both model runs agree with the pattern in NCEP reanalysis (Fig. 6d). The STD pattern of the intraseasonal precipitation (Fig. 6e) is similar to the pattern in Fig. 6a. Over the tropical Pacific Ocean, the double ITCZ problem still exists in C3NEW, although there is moderate improvement in contrast with C3OLD (note the negative anomalies around 10°S in the central Pacific in Fig. 6c). It was argued in Neale et al. (2008) that the current changes in the convection scheme are not very helpful for removing the southern Pacific convergence zone (SPCZ) bias. Another notable difference between the two runs (Fig. 6c) is the reduced precipitation from the tropical Indian Ocean to the western tropical Pacific Ocean, the region in which the ISVs are actually stronger in C3NEW than those in C3OLD (Fig. 5d). It is also true that the STDs of the intraseasonal precipitation in C3NEW are smaller than those in C3OLD over the tropical region (Fig. 6f). Since precipitation is the product of convection, the mean vertically averaged deep convective heating (product of the Zhang–McFarlane scheme) in C3NEW (Fig. 7a) has almost the same structure as precipitation does (Fig. 6a). In addition, the reduction in convective heating from the Indian Ocean to the western Pacific Ocean is also obvious in Fig. 7b. In the intraseasonal band (20–100 days), the STDs of convective heating in C3NEW (Fig. 7c) are also smaller than those in C3OLD (Fig. 7d), which are consistent with Figs. 6e and 6f. The vertical profiles of convective heating (averaged between 5°N and 5°S) are shown in Fig. 8. The general pattern in the two model runs are similar, both of which are consistent with Tropical Rainfall Measuring Mission (TRMM) data (http://disc.sci.gsfc.nasa.gov/precipitation/documentation/ TRMM_README/TRMM_CSH_readme.shtml). Although TRMM data include both convective heating and stratiform heating, convective heating dominates over the tropics. The major features of the observed heating profile are captured by the model; for instance, the intensive heating occurs in the midtroposphere over the oceans. But, the pressure level with maximum convective heating in the model seems a little lower than observations. The differences in vertical heating profiles between the two model runs are shown in Fig. 8c. Convective heating in C3NEW is smaller than that in C3OLD in both low level (~900 hPa) and midlevel (~500 hPa) from the Indian Ocean to the western Pacific Ocean, consistent with the vertically averaged heating shown in Fig. 7b. By examining the convective heating in C3DPA and C3CMT, one can see the reason for the reduction of convective heating in the upper two levels in C3NEW. As a product of the convective parameterization (Fig. 9a), humidity (Q) tends to decrease, driven by condensation and subsidence in the lower levels (below 800 hPa). Actually, in the midtroposphere, there is also a decreasing tendency for humidity, but the amplitude is much smaller than in the lower level. Note that the Q tendency shown in Fig. 9 is only the tendency due to convection, rather than the total tendency. After adopting DPA, moisture condensation becomes weaker and the dry tendency decreases in the boundary layer around 900 hPa and the midtroposphere around 500 hPa (positive values
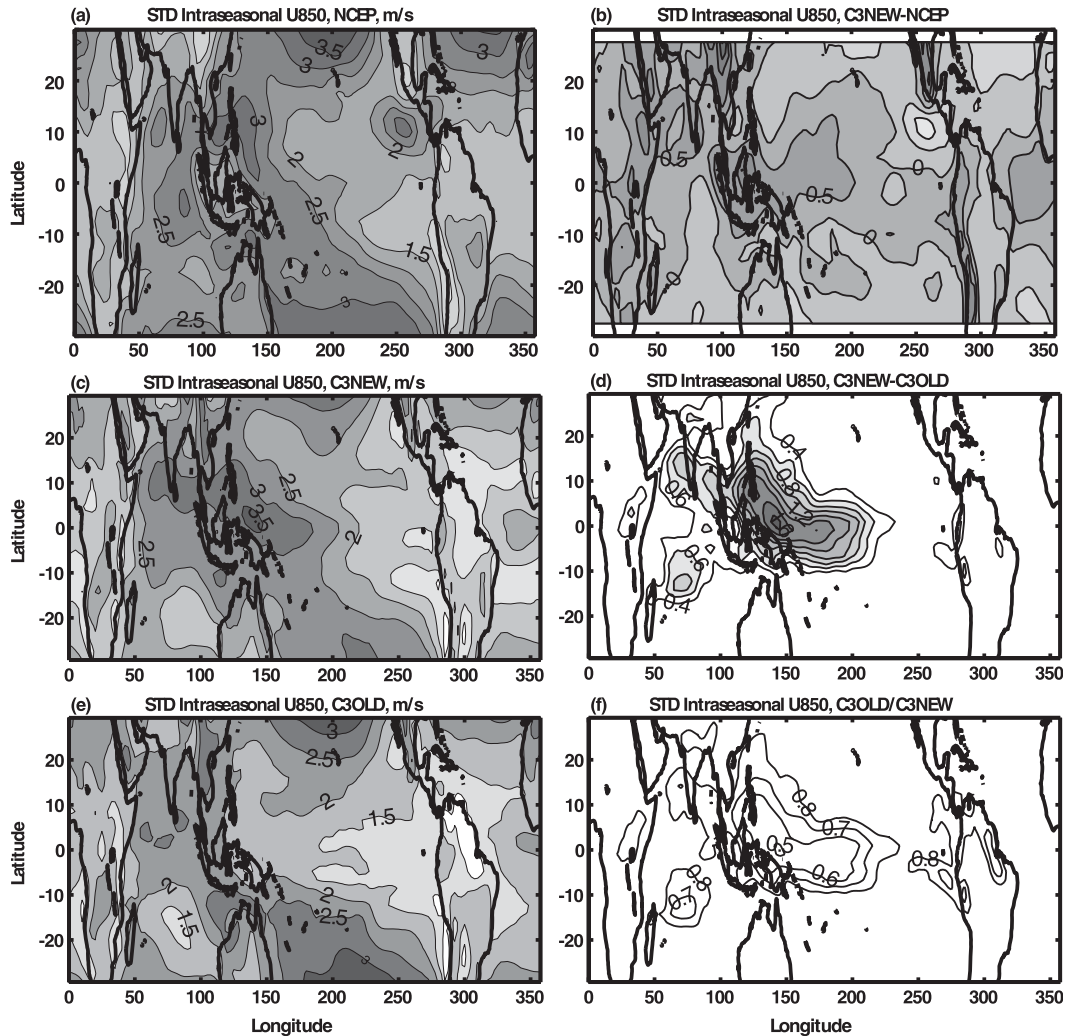
FIG. 5. STDs of intraseasonal zonal winds at 850 hPa in (a) NCEP from 1979 to 2009, (c) C3NEW, and (e) C3OLD; the STD differences between (b) NCEP and C3NEW and (d) C3NEW and C3OLD as well as (f) the ratios C3OLD/C3NEW are shown.

in Fig. 9b) because the mixing between rising air parcels and ambient (relatively dry) air happens at all levels of the convective plume, not only at the cloud top. As a result, the convection is suppressed [too frequent convection is a common problem in MJO simulations, Lin et al. (2006)] and the convective heating decreases at these two levels (Fig. 9e). Especially, the changes in convective heating from C3OLD to C3DPA in Fig. 9e are very similar to the changes in Fig. 8c (between C3NEW and C3OLD), which indicates that the modification in convective heating in C3NEW is mainly due to DPA. In contrast, after adopting CMT, the changes in the Q tendency comparing with C3OLD are small (Fig. 9d). Thus, the significant reduction in negative Q tendency in the lower level in C3NEW (Fig. 9c) is mainly attributable to DPA. Correspondingly, the changes in convective heating from C3OLD to C3CMT

are also relatively small in the midtroposphere (Fig. 9f) from the Indian Ocean to the western Pacific Ocean, which is the major region of MJO activity. No distinct variation can be seen in the boundary layers.

However, as emphasized in Emanuel et al. (1994), convective heating is not the only determining factor for the strength of ISVs; in addition, the correlation (or the phase relation) between convective heating and the temperature perturbation is also a key factor. The thermodynamic equation can be approximately written as

$$\frac{\partial T'}{\partial t} - w' S_p \approx \frac{J'}{C_p}, \qquad (2)$$

where T is the air temperature, w the vertical pressure velocity, S_p the static stability parameter, and J is
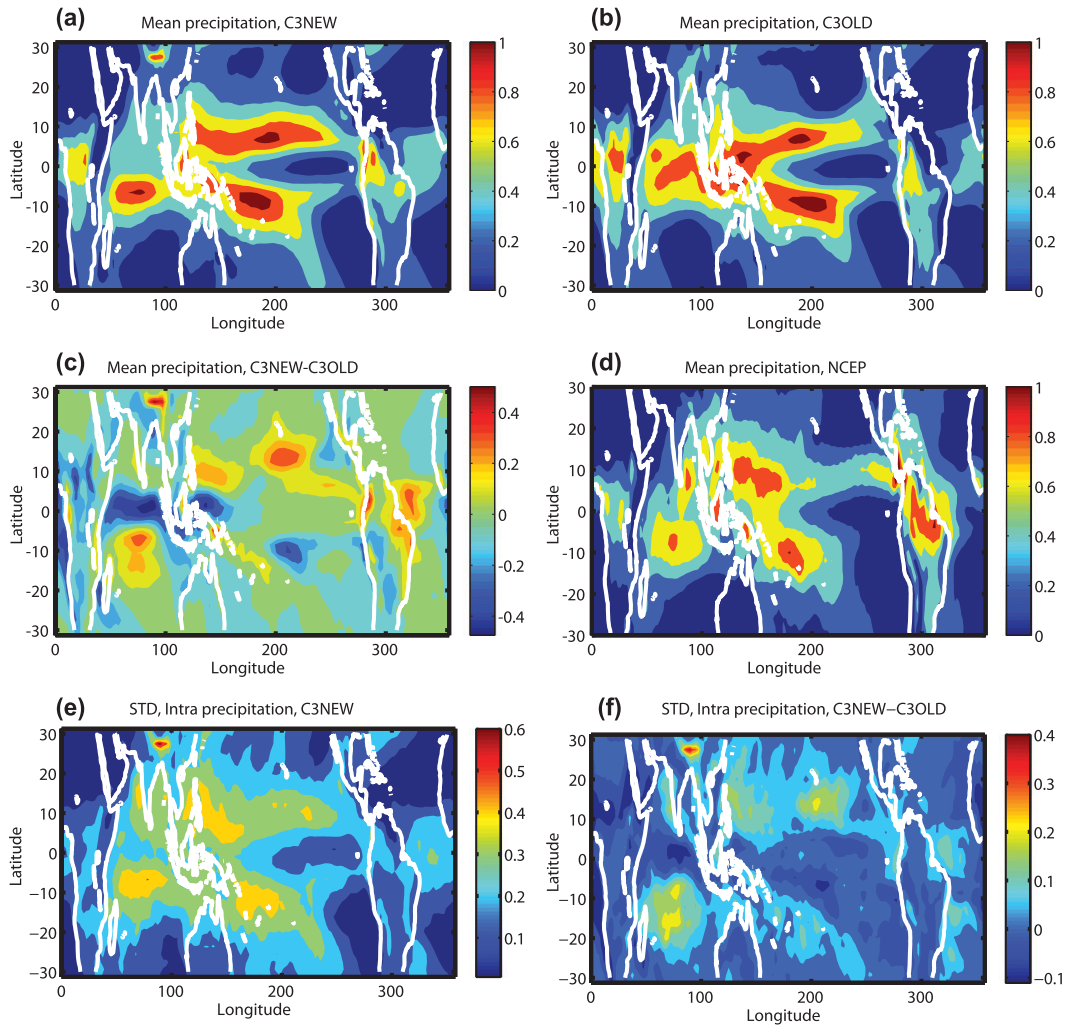
FIG. 6. Mean precipitation (cm day^{-1}) in (a) C3NEW, (b) C3OLD, and (d) NCEP reanalysis from 1979 to 2009. (c) The differences between C3NEW and C3OLD are shown. (e) The STDs of the intraseasonal precipitation in C3NEW and (f) the differences of the STDs of the intraseasonal precipitation between C3NEW and C3OLD.

convective heating, which is the major component of the total external heating; C_p is the heat capacity of the air, and the prime denotes the intraseasonal component (between 20 and 100 days) of the variables. Since some terms are neglected in the above thermodynamic equation (such as the advection terms), we use "≈" instead of "=". Multiplying by T' on both sides of Eq. (2), one obtains

$$\frac{\partial}{\partial t}\left(\frac{T'^2}{2}\right) - T'w'S_p \approx \frac{T'J'}{C_p}, \quad (3)$$

where $T'^2/2$ is proportional to the available potential energy in the intraseasonal band, $T'J'$ is critical to the buildup of available potential energy during convection, and $-T'w'$ determines the energy conversion from available potential energy to kinetic energy. Although

the two terms, $T'J'$ and $-T'w'$, are different at a given position or at a given time between the two model runs, usually the averages of these two terms over a large enough spatial domain and a sufficiently long time (compared with the spatial and temporal scales of perturbations) are physically meaningful. In addition, the average of $T'J'$ $(-T'w')$ over a long time largely depends on the phase relation between T' and $J'(w')$. Similar to the method used in Slingo et al. (1999), we calculate the mean variance of J' and T' (vertically averaged from 1000 to 200 hPa, then averaged from 10°S to 10°N, 50° to 100°E and passed through a 101-day running mean; see Fig. 10). The variance of convective heating is virtually indistinguishable between the two runs (the 20-yr mean of J' variance is 1.23×10^{-11} K s^{-1} in C3NEW and 1.37×10^{-11} K s^{-1} in C3OLD), which is consistent with Fig. 7, although the
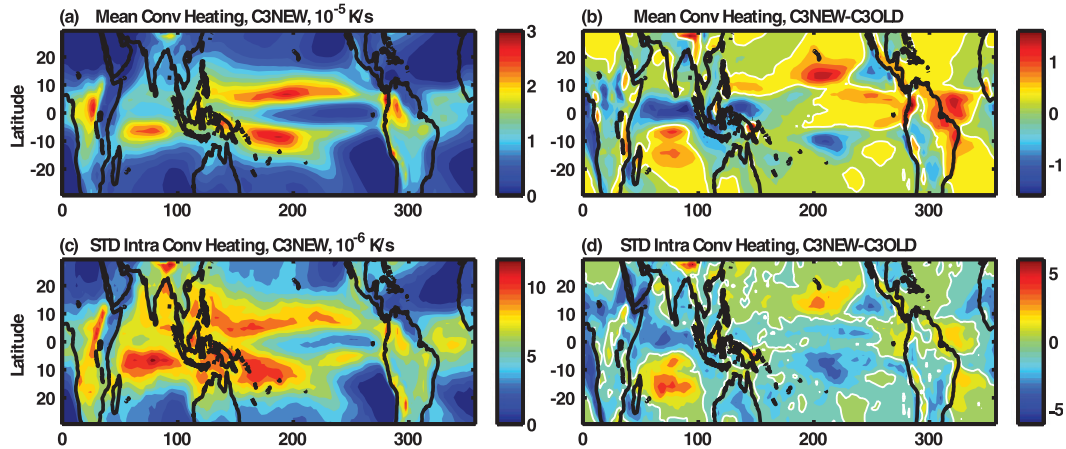
FIG. 7. Twenty-year mean (a) convective heating in C3NEW and (b) the difference between C3NEW and C3OLD. STDs of (c) the intraseasonal convective heating in C3NEW and (d) the difference between C3NEW and C3OLD. The white contours correspond to zero.

spatial distribution and phase of J' are different in the two runs. The temperature variance is larger in C3NEW than in C3OLD (Fig. 10b), consistent with the normalized differences in temperature in the two runs (Fig. 3b). In contrast, positive $T'J'$ (Fig. 10c) and positive $T'w'$ (Fig. 10d) in C3NEW clearly have higher peaks than that in C3OLD, which explains the more energetic ISVs in the former run. The correlations between $T'J'$ and the MJO index (Fig. 4) are around 0.3 for both C3NEW and C3OLD, which is statistically significant at a confidence level of 99%. Note

that the mean value of $T'J'$ over a large domain (larger than the spatial and temporal scales of the perturbations) depends more on the phase relation between the two perturbations than on the amplitudes of the perturbations at a specific location or a specific time. Thus, the peaks in $T'J'$ (Fig. 10c) are not consistent with the large values in T' (Fig. 10b), which indicates that the peaks in $T'J'$ are not due to larger T' in C3NEW (which is probably attributable to the energy imbalance over the whole globe for the 20 years), but due to the modified phase relation between T'
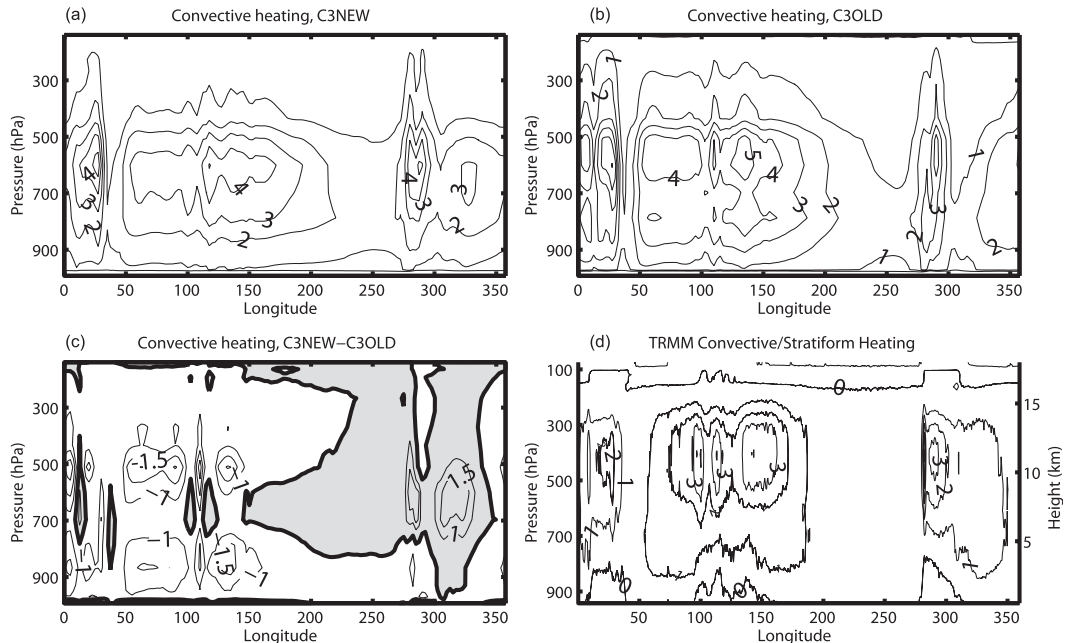

FIG. 8. Vertical profile of mean convective heating (10^{-5} K s^{-1}) over 20 years, averaged between 5°N and 5°S for (a) C3NEW and (b) C3OLD. (c) Differences of the mean convective heating between C3NEW and C3OLD, positive differences shaded. (d) Mean TRMM heating products from 1998 to 2009, averaged between 5°N and 5°S.
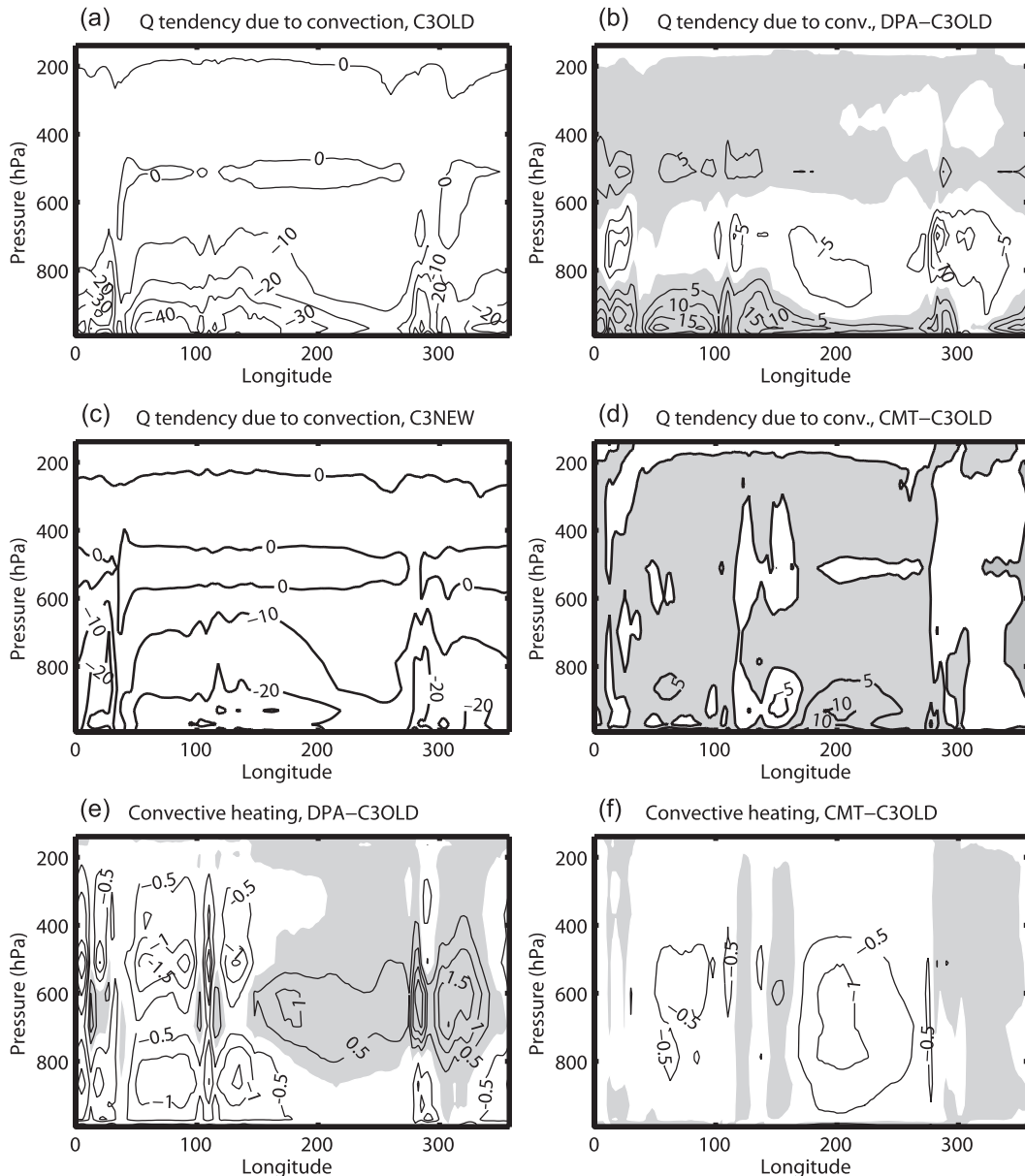
FIG. 9. Humidity (Q) tendency (10^{-9} kg kg^{-1} s^{-1}) due to convection (a) in C3OLD and (c) in C3NEW and differences (b) between C3DPA and C3OLD and (d) between C3CMT and C3OLD. Differences in convective heating (10^{-5} K s^{-1}) (e) between C3DPA and C3OLD and (f) between C3CMT and C3OLD.

and J' in C3NEW. The model performance is thus consistent with the principle of the quasi-equilibrium theory for convection (Emanuel et al. 1994). Due to DPA, the environmental air is entrained into the cloud at all levels, not only at cloud top (Raymond and Blyth 1986). As a result, the phase relations between the convective heating and the temperature perturbation are modified. Although the convective heating is generally a little weaker because of the entrainment of dry air in C3NEW than it is in C3OLD (Figs. 7 and 8), both the buildup of potential

energy ($T'J'$, Fig. 10c) and the release to kinetic energy ($-T'w'$, Fig. 10d) become larger in C3NEW. Therefore, the ISVs in C3NEW are stronger than those in C3OLD.

4. Organization of the intraseasonal variabilities

a. Composite MJO phases

Differences between the two model runs reside in the propagating features of the ISVs. The ISVs in C3NEW are not only more energetic, but also better organized in
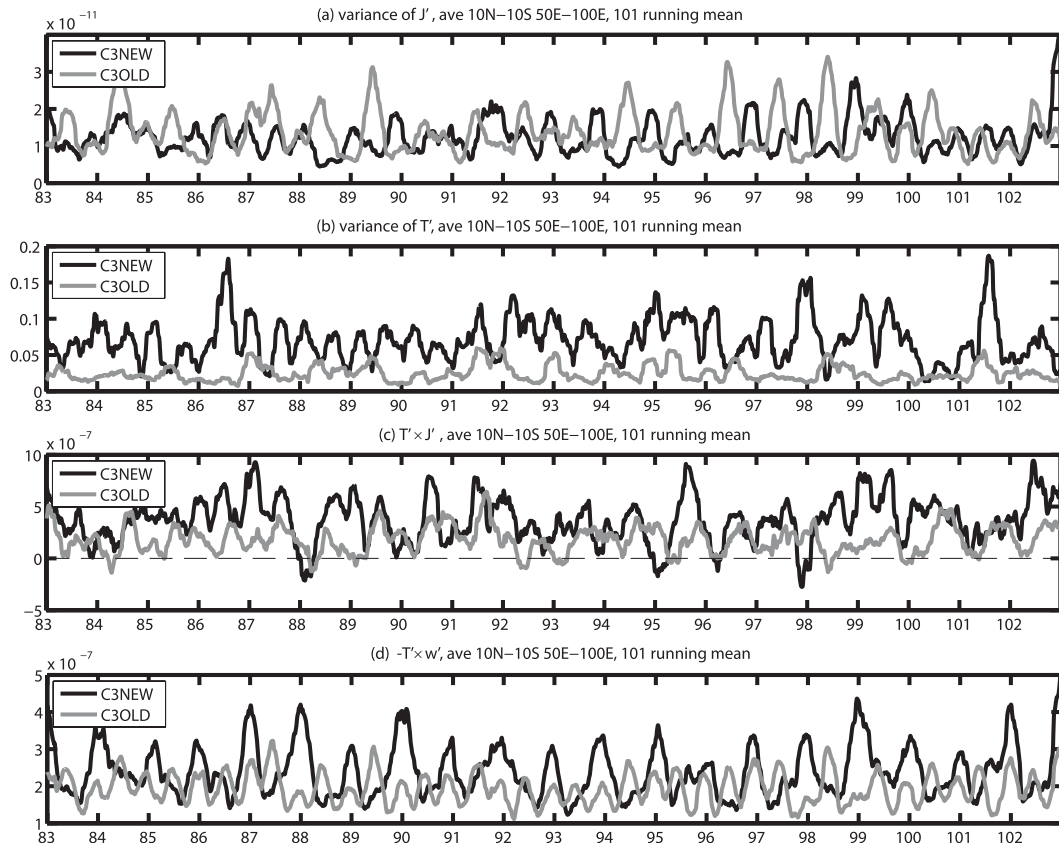
FIG. 10. Variance (a) of J' (K s^{-1}), (b) of T' (K), (c) of T' J' (K^2 s^{-1}), and (d) of T' w' (K Pa s^{-1}) averaged in the vertical from 1000 and 200 hPa within 10°S–10°N, 50°–100°E, then passing a 101-day running mean.

comparison to the reanalysis. Thus, they resemble the observationally inferred MJOs much more so than the ISVs in C3OLD.

Observed MJOs are composed of successive suppressed and active phases during the eastward propagation (Zhang 2005). Thus, with the EOF analysis, the first two EOF modes are in quadrature, which is represented with the significant cross-correlation at a time lag of 10–15 days between the principal components (PCs) of the first two EOFs. This relation is well captured in C3NEW in the intraseasonal zonal winds at both 200 and 850 hPa, and for the intraseasonal OLR anomalies, while it is not as well captured in C3OLD (Fig. 11). For comparison, the cross-correlation for zonal winds at 200 and 850 hPa, which are obtained from NCEP reanalysis, and OLR from the NOAA satellite OLR data (Liebmann and Smith 1996) are superimposed in the corresponding panels in Fig. 11. Better coherence between the first two modes of the EOFs of intraseasonal zonal winds and OLR indicates a better eastward propagation of the ISVs during MJOs, which continues to be a major challenge for MJO simulations. The ISVs in C3OLD, although they can be energetic, do not have such coherent eastward propagation. In addition,

the first two EOF modes in C3NEW explain about 14% of the total variance of the intraseasonal zonal winds at 850 hPa and about 16% of the total variance at 200 hPa, which are comparable with the observations (13%–16%). As summarized in the Working Group, "many climate (model) simulations produce leading EOFs for convective fields that explain relatively small amounts of the variance compared to observations" because the ISVs in many models were likely to be strong enough but not organized well enough. Cross-correlations between the first two EOFs for C3CMT and C3DPA are also shown in Fig. 11. Although the ISVs in C3CMT are slightly weaker than the counterparts in C3DPA (Fig. 4b), the quadrature relation is better captured in C3CMT, which implies that the CMT is more conducive to the organization of the ISVs. However, the first two EOFs in C3CMT only explain about 6% and 5%, respectively, of the total variance in the intraseasonal band because the organized ISVs are weak due to the absence of DPA.

Following Wheeler and Hendon (2004), the MJO phases can be defined with the first two PCs of the multivariate EOF analysis (based on OLR, zonal winds at 850 and 200 hPa) and the phase diagram using daily
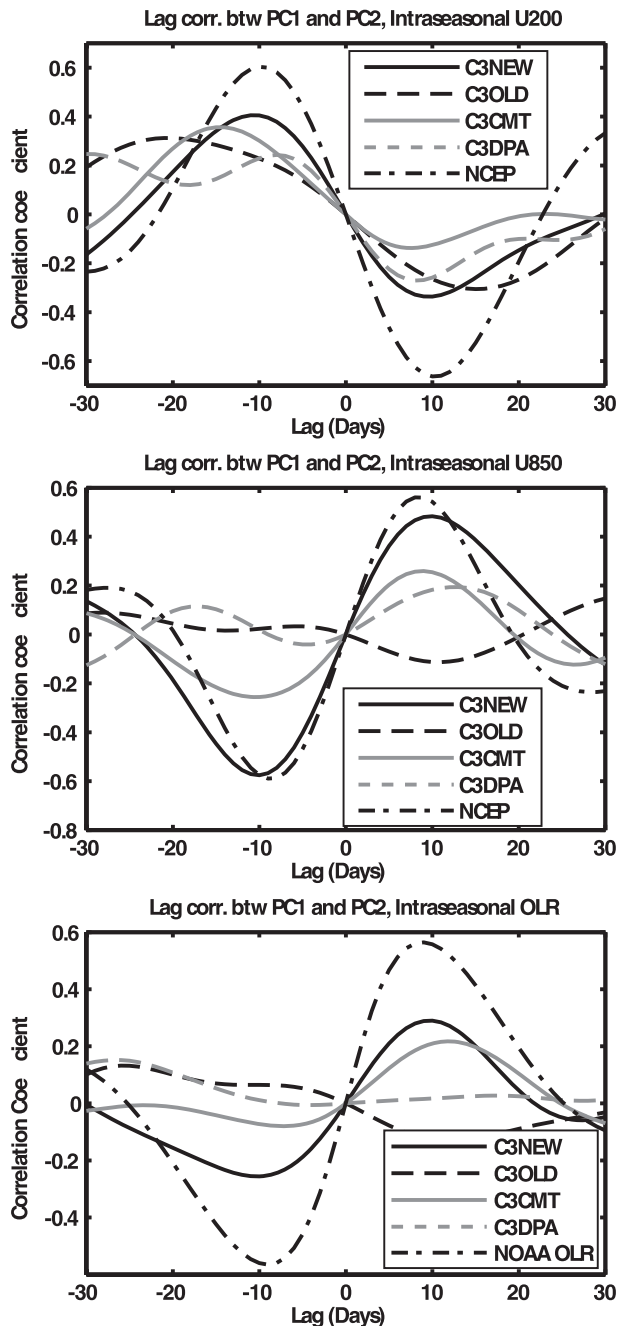
FIG. 11. Cross-correlations between PC1 and PC2 of the intraseasonal zonal winds (top) at 200 hPa and (middle) at 850 hPa and (bottom) intraseasonal OLR anomalies. Cross-correlations between PC1 and PC2 of the intraseasonal zonal winds at 200 and 850 hPa from NCEP (from 1979 to 2009), and intraseasonal OLR from NOAA polar-orbiting series of satellites (from 1979 to 2009) are superimposed in corresponding panels.

outputs is shown in Fig. 12. Note that, being different from the MJO index shown in Fig. 4, no running mean is applied to Fig. 12. The ISVs are regarded as strong when $(PC1^2 + PC2^2)^{1/2}$ is larger than $\sqrt{2}$. Canonically, an MJO

event originates from the western Indian Ocean and diminishes over the eastern Pacific Ocean. Thus, the line rotates counterclockwise in the phase diagram. Six MJO events are defined based on the strength of the ISVs [represented with $(PC1^2 + PC2^2)^{1/2}$] and the eastward propagation (the phase diagram shown in Fig. 12a), which are listed in Table 3. For comparison with reanalysis, the phase diagram of four observed MJO events is shown in Fig. 12b. The number of MJO events appears to be fewer than those in the reanalysis in a typical year. One important reason is that we intend to guarantee that all selected MJO events can travel continuously around the globe from the western Indian Ocean back to the Western Hemisphere since we want to focus on the eastward propagation of ISVs in the following discussion. Thus, the selected MJO events are required to show smooth counterclockwise rotation in the phase diagram as shown in Fig. 12. This criterion is much stricter than only requiring large amplitudes, like $(PC1^2 + PC2^2)^{1/2} > \sqrt{2}$.

The ISVs in C3NEW propagate eastward (Figs. 11 and 12) and resemble realistic MJO events, while the ISVs in C3OLD barely propagate, although they are enhanced occasionally (Fig. 4). Naturally, the question is what leads to the eastward propagation of the enhanced ISVs in C3NEW and, more specifically, what determines the eastward propagation speed of MJOs? Since the improved simulation of background low-level winds from the tropical Indian Ocean to the western Pacific Ocean is the most significant modification between C3OLD and C3NEW (Figs. 2 and 3), it should be a candidate to explain the better organization of ISVs in C3NEW.

b. Eastward propagation of MJOs

Several mechanisms have been proposed to explain and to capture the slow movement of the MJO events over the Indo-Pacific warm pool, which is much slower than the free planetary waves. A friction–convergence mechanism was invoked to account for the retardation in the eastward propagation of MJO events (Wang and Rui 1990; Salby et al. 1994). However, the drag coefficients used in the friction–convergence theory were deemed to be unrealistically large, such that the actual role of friction was also debatable (Sperber et al. 1997; Moskowitz and Bretherton 2000). In a numerical model study, Chao and Chen (2001) showed that friction may not be as important as claimed for the low-level convergence. Instead, friction only dissipates the energy of MJOs. Studies have also shown that the enhanced surface heat flux could determine the speed of the eastward propagating ISVs, as hypothesized in the wind-induced surface heat exchange (WISHE) theory (Emanuel 1987; Neelin et al. 1987). However, the easterly winds to the east of convection required by the linear WISHE mechanism have been proven to be unrealistic

TABLE 3. MJO events defined with the C3NEW outputs.

Event	Year	Day
1	101	52–86
2	99	27–54
3	96	65–114
4	91	39–91
5	90	60–120
6	84	65–126

As described above, the generation of available potential energy and kinetic energy during convection is determined by $T'J'$ and $-T'w'$. Actually we can treat $T'J'$ and $-T'w'$ in a similar way when assessing the circumstances under which these two terms have significantly nonzero values. According to the weak temperature gradient approximation (Sobel et al. 2001; Bretherton and Sobel 2002), which was thoroughly tested for applications in the tropical ISVs (Bretherton and Sobel 2003), variation of T' with longitude is small and the principal thermal–dynamical balance is $-w'S_p = J'$, where S_p is the static stability parameter. Since S_p is a slowly varying quantity, w' and J' have similar structures. The weak temperature gradient and similar structures between w' and J' are also reproduced in C3NEW. As shown in Fig. 13, the variation patterns of J' and w' are similar and the variation of T' along a latitude is quite small compared with the variation of J' and w'. There is a blank region in the tropics in Fig. 13a, which is the region of essentially uniform T' covered by the minimal STD of T' (0.23 K). To quantify the above argument, we calculate the ratio $STD(X_{lat})/mean(X_{lat})$, along every latitude where X_{lat} represents the STD of vertically averaged T', J', and w' (from 1000 hPa to 200 hPa) along each latitude shown in Figs. 13a,c,e. The ratios are shown on the right column of Fig. 13. The patterns in Fig. 13 remain similar if one makes such a figure with the variables on a lower level, such as 850 hPa. For T' the zonal variance is less than 10% of the zonal mean, while for J' and w' the zonal variance is about 20%–60% of the zonal mean. Therefore, the zonal oscillatory parts of $T'J'$ and $-T'w'$ are determined by J' and w', respectively. Here J' and w' are composed of oscillations with various wavenumbers and frequencies (Wheeler and Kiladis 1999) and each component can be written in a wavelike form, that is, $A(k)e^{it\psi}$, where $\psi = kU - \omega(k)$ and $U = x/t$ is the mean zonal current. In contrast, since the variance of T' is very uniform in the zonal direction (Fig. 13a), it is not necessary to decompose T' into various wavenumber components. Thus, $T'J'$ can be expressed as the sum of the waves with all wavenumbers (the same argument can also be applied to $T'w'$),
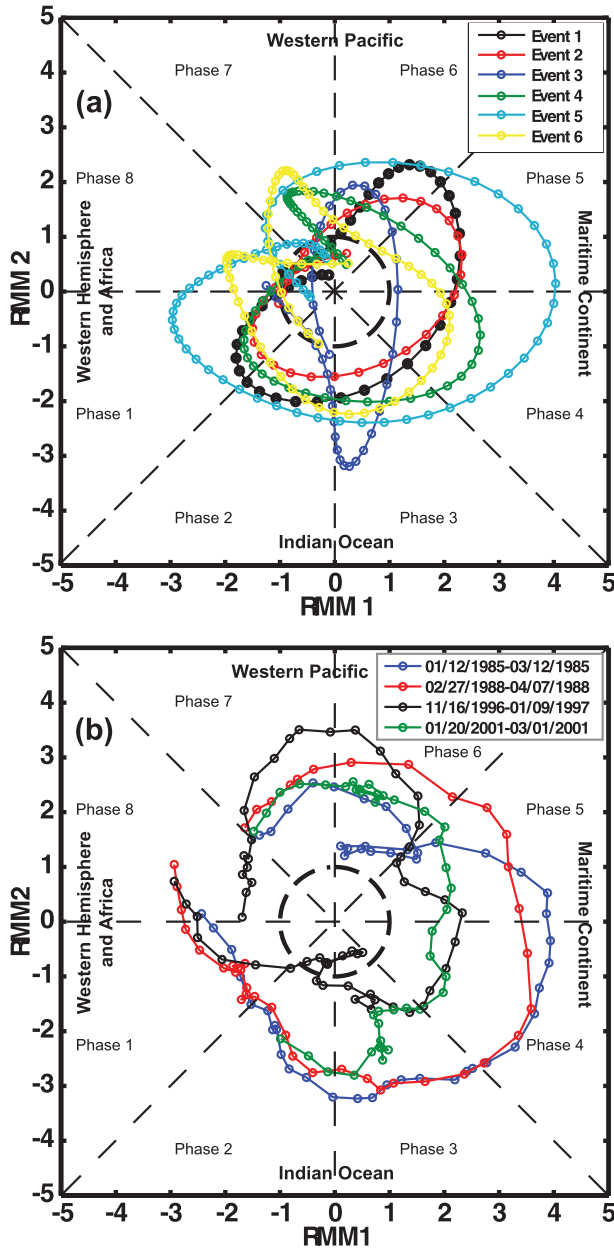
FIG. 12. Phase diagram in terms of (a) the first two PCs of the EOF analysis for 6 MJO events in C3NEW listed in Table 3; every curve rotates anticlockwise. The dash cycle is the unit cycle. (b) As in (a) but for four observed MJO events, which are used again in Fig. 15.

against observations. In practice, a weak, rather than a strong, evaporation usually leads convection (Woolnough et al. 2001). Furthermore, it is nontrivial to explain why most MJO events "select" to travel around 5 m s^{-1}, rather than a random speed over a wider range. With our model simulations and NCEP reanalysis, we argue below that the large-scale zonal winds are likely to play a role in pacing the eastward speed of MJOs.
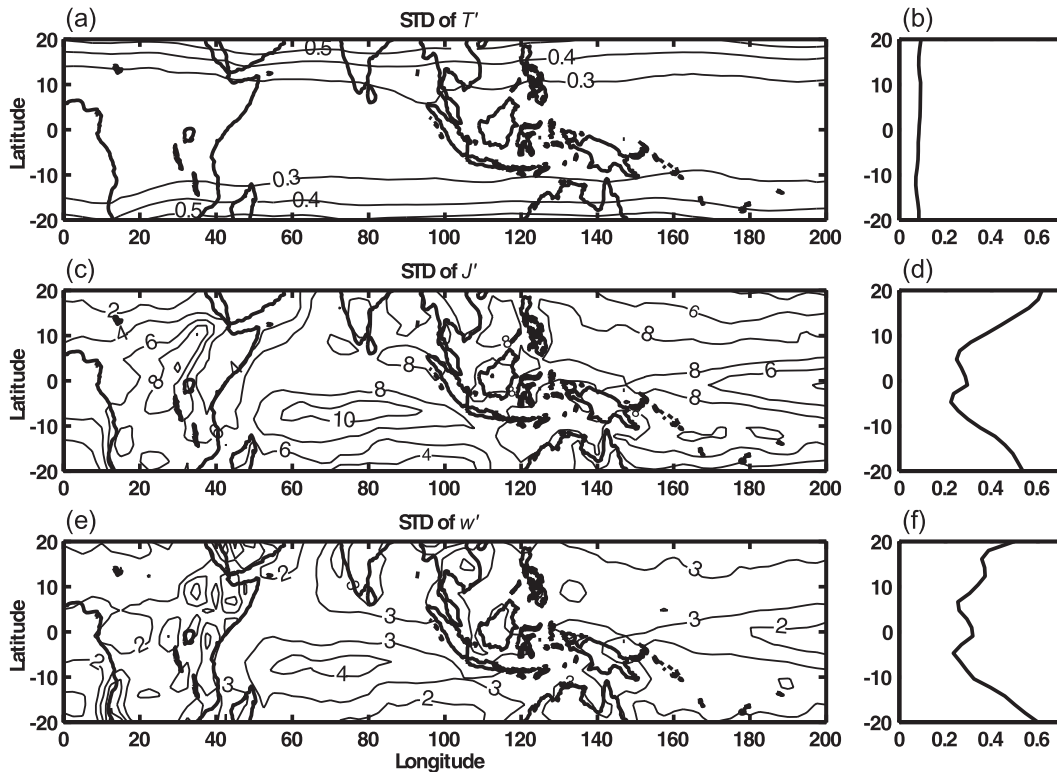
FIG. 13. STD of (a) intraseasonal temperature (K), (c) convective heating J' (10^{-6} K s^{-1}), and (e) vertical velocity w' (10^{-2} Pa s^{-1}). Ratios of STD(X_{lat})/mean(X_{lat}), where X_{lat} represents the STD of T', J', and w' along every individual latitude shown in the left column, are plotted in the right column.

$$T'J' = T'\int_0^\infty A(k)e^{it\psi}\,dk. \qquad (4)$$

Then integration by parts yields

$$T'J' = T'\int_0^\infty \frac{Ae^{it\psi}}{d\psi/dk}\,d\psi$$

$$= \frac{T'}{it}\frac{Ae^{it\psi}}{d\psi/dk}\bigg|_0^\infty - \frac{T'}{it}\int_0^\infty e^{it\psi}\,d\psi\frac{d}{d\psi}\left(\frac{A}{d\psi/dk}\right). \qquad (5)$$

Equations (4) and (5) are valid both for the vertically integrated perturbations (as shown in Fig. 13) and for the perturbations on a lower level (e.g., at 850 hPa). According to the method of stationary phase [see Pedlosky (2003) for details], the term

$$\frac{T'}{it}\frac{Ae^{it\psi}}{d\psi/dk}\bigg|_0^\infty$$

decreases with $1/t$ and approaches zero after a considerable period of time (when t is large). The last term in Eq. (5) also decreases at least as fast as $1/t$, unless $e^{it\psi}$ does not oscillate too rapidly at large t. Here large t means that the time is longer than the time scale of

perturbations. Physically, t is the time that random perturbations need to get adjusted or organized; thus it is longer than the time scale of perturbations themselves. For the current study, the perturbation is on the time scale of convective systems, which is O(days). Thus, the time scales of MJOs and background state are much longer than O(days) and, over this period, time t can be regarded as long enough. At large t, $T'J'$ has a significantly nonzero value only when ψ does not change, in other words, at the stationary point of ψ with respect to k. Thus, $\partial\psi/\partial k = 0$ is a necessary condition and the group velocity of perturbations is $C_g = \partial\omega/\partial k = U$. This relation implies that the propagation speed of the perturbations, which can last for a long time, is not determined by the mesoscale variability itself. Instead, it is selected by the background zonal flow. Note that we do not argue that the ISVs are simply advected by the mean flow. Actually, the fluctuations caused by an individual convective event can have a considerably different propagation speed from the background state (Hendon and Liebmann 1994; Wheeler and Kiladis 1999). These fluctuations can be very energetic in the spatiotemporal scales of tropical convection (on the order of days and hundreds of kilometers) but tend to dissipate on much

larger spatiotemporal scales (e.g., the scale of MJOs, on the order of tens of days and thousands of kilometers) because they have random phases that are prone to cancel each other (the physical essence of the method of stationary phase). Only the fluctuations that have a coherent relation with the background state can last for a long time and propagate over large distances. This process is analogous to a selective conveyor belt (the background state), which selectively picks only the suitable perturbations and discards (dissipates) the unfitting ones, organizing the former into an energetic event that is much larger in space and longer in time than any individual perturbation. As a result, one can observe the well-organized MJO events, which originate from the unorganized deep convection but have much larger space scales and much longer time scales than any individual deep convective cell.

The above arguments are supported by evidence from both our model simulations and the NCEP reanalysis. Intraseasonal OLR anomalies during two simulated MJO events are shown in Figs. 14a and 14b. The ISVs propagate eastward at a speed of about 4 m s^{-1}, as indicated with the gray dashed lines. Contours of the background zonal winds (passed through a low-pass filter with a cut-off period of 100 days) at 4 m s^{-1} at 850 hPa are superimposed. The eastward propagation speed of ISVs is consistent with the background zonal wind speed. A caveat for current model results is that the initial states of MJOs are not very well simulated. Actually, simulation of the onset stage of MJOs is still a big challenge for models. Thus, in Fig. 14, the propagating signals are not clear to the west of 100°E. But, with NCEP reanalysis (see below), one can see the propagation of MJOs at the early stage clearly. As shown in Fig. 4, there are also pronounced ISVs in C3OLD, but they do not propagate to the east (see the flat lag-correlation coefficients in Fig. 11). Intraseasonal OLR anomalies from the end of year 95 to the beginning of year 96 in C3OLD are shown in Fig. 14c (negative days in Fig. 14c are days in year 95 with respect to day 1 in year 96). Strong negative OLR anomalies in the central Indian Ocean (~100°E) are obvious and are comparable with those in C3NEW in strength. The negative OLR anomalies during the periods in Figs. 14a and 14b are not as strong as the ones during the period in Fig. 14c. However, the background zonal winds are very weak during this period of time and the negative OLR anomalies in C3OLD do not propagate to the east. Therefore, the most reasonable explanation is that the distinctive difference in the eastward propagation of ISVs in the two model runs is attributable to the difference in the simulations of the large-scale zonal winds. This hypothesis is also supported when one considers

OLR observations and NCEP reanalysis. Figure 15 shows the intraseasonal OLR anomalies [obtained from NOAA polar-orbiting series of satellites, Liebmann and Smith (1996)] during four MJO events, superimposed on the zonal background velocities (from NCEP reanalysis, low-pass filtered at 100 days). The propagation speeds of the intraseasonal OLR anomalies, marked with gray lines, range from 4 to 4.7 m s^{-1}. The speeds are consistent with the zonal background speeds. Actually, the MJO speed is not exactly 5 m s^{-1}. Statistics in Jones (2009) showed that the MJO speed ranges from 0.7 m s^{-1} to 5.1 m s^{-1} with a STD of 0.9 m s^{-1}. The background wind speed also has variance, which is roughly comparable with the variance of the MJO phase speed from the central Indian Ocean to the western Pacific Ocean (not shown). The four examples shown in Fig. 15 occur from November to May, which cover the whole period of boreal winter. We do not give examples in boreal summer since it is well known that the ISVs in boreal summer have some special features, such as the northward propagation that is supposed to be related to the warm SST anomalies over the Bay of Bengal. In addition, one can estimate the group velocities of the high-frequency tropical waves from their dispersion relation (such as the Wheeler–Kiladis diagram, Wheeler and Kiladis 1999). It can be shown that the high-frequency waves with a speed ~5 m s^{-1} exist. Thus, both observations and our simulations confirm that the eastward propagation speeds of MJOs are consistent with the background zonal wind speed, although both MJO speed and background wind speed have some variance.

The above arguments only apply to the warm pool region from the central Indian Ocean to the western Pacific Ocean (50°E–180°), where convective heating is pronounced (Fig. 8) and thereby $T'J'$ is a significant external forcing. Consistently, this region is also the region with improved westerly winds (Fig. 2). In contrast, from the central to the eastern Pacific Ocean where easterly winds dominate, J' and $T'J'$ become much weaker due to the cooler equatorial SSTs. As a result, MJOs become more like free Kelvin waves, which have a faster speed than they are over the warm pool region. Moreover, as shown in Figs. 9 and 10, major differences in J' between C3NEW and C3OLD occur in the low level and midlevel, while J' in the upper layer is relatively small. Thus, the different MJO simulations in the two runs should be attributable to the modification in the external forcing of J' at a lower level. Although the effect of background zonal winds is highlighted in the above analysis, it does not mean that MJO propagation is only determined by the dynamic processes. Actually, $T'J'$ analyzed in Eq. (4) is closely related to the thermodynamical processes (e.g., the convective
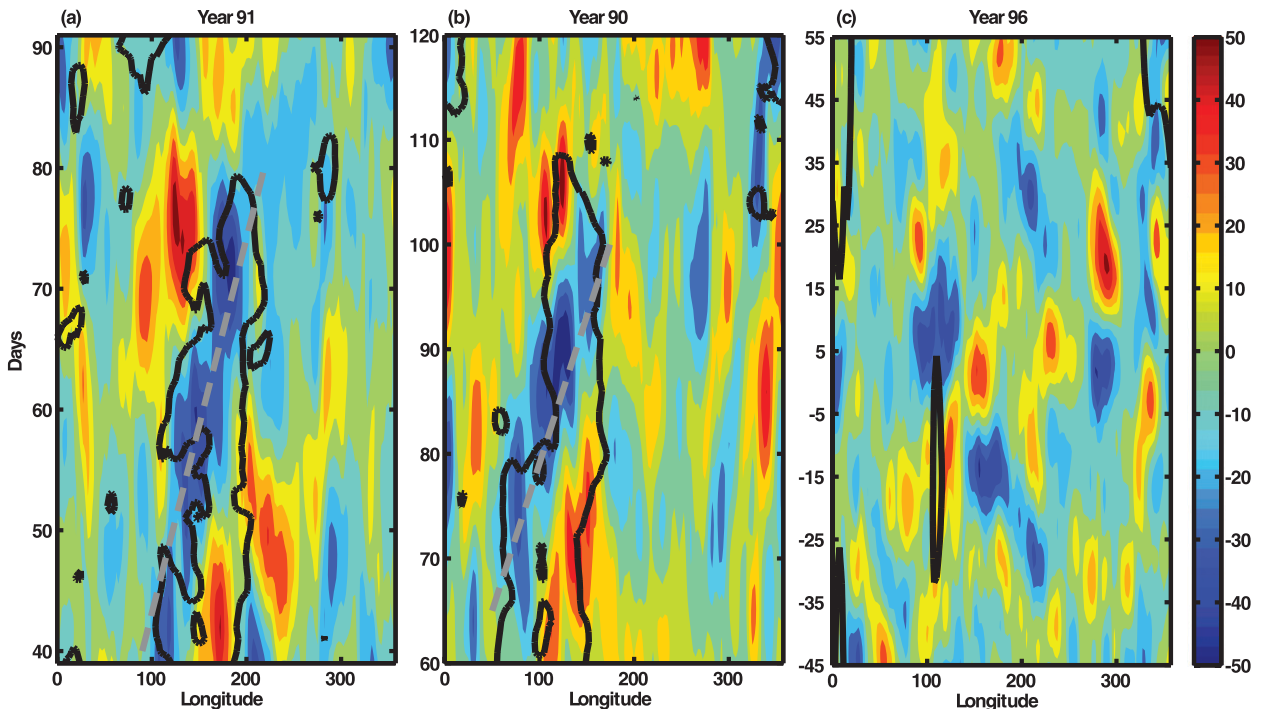
FIG. 14. Intraseasonal OLR anomalies (W m^{-2}) (color shades) averaged between 10°N and 10°S during (a),(b) two MJO events in C3NEW (Table 1). The gray dash lines mark an eastward propagation speed of 4 m s^{-1}. The black contours represent the background zonal winds (after a low-pass filtering of 100 days) of 4 m s^{-1} in the same region. (c) As in (a) but when the ISVs are strong in C3OLD. The black contours also represent the background zonal winds of 4 m s^{-1} in the same region.

heating J'). The above analysis also applies to $-T'w'$ because of the balance between J' and w', and $-T'w'$ represents a dynamical process. Therefore, the MJO propagation is a combined result of both thermodynamical and dynamical processes.

The above analyses can help us understand why the eastward propagation of ISVs in C3NEW is better than those in C3OLD. As shown in Fig. 2, the background westerly winds are pronounced at ~5 m s^{-1} in C3NEW from the tropical Indian Ocean to the western Pacific Ocean. As a result, in C3NEW and C3CMT, the ISVs are better organized by the large-scale flow and propagate eastward, which is represented with the cross-correlation between the PCs of the first two EOFs shown in Fig. 11 (especially for the intraseasonal zonal winds at 850 hPa and for intraseasonal OLR anomalies) and the phase diagram in Fig. 12. In contrast, in C3OLD and C3DPA, there are almost no background low-level westerly winds over the Indo-Pacific warm pool. Therefore, although the ISVs can be enhanced by the Zhang–McFarlane deep convection parameterization scheme (Zhang and Mu 2005) and DPA, their eastward propagation tends to be rather weak. Instead, the ISVs are mostly generated as well as dissipated locally (Fig. 14c). As a result, there is no significant cross-correlation between the first two EOF

PCs (Fig. 11), which indicates a lack of eastward propagation.

5. Conclusions and discussion

Two modifications are made to the convection scheme in the CCSM3 model, which led to a better simulation of MJOs. The reduced easterly wind bias from the Indian Ocean to the western Pacific Ocean is the most significant change induced by the modifications to the Zhang–McFarlane scheme. In a coupled system, the postadjustment states may well appear proximate but the adjustment process itself may produce more distinguishable responses, as in the strength and propagation of MJOs for the cases under consideration here. Inclusion of a dilute plume approximation (DPA) improves the correlation between J' and T', which is critical for the buildup of the available potential energy. Although the convective heating is indistinguishable between C3NEW and C3OLD, $T'J'$ is much larger in C3NEW. Since w' has a similar structure to J', $-T'w'$ is also larger in C3NEW, which makes the energy conversion from available potential energy to kinetic energy more efficient. As a result, intraseasonal variabilities (ISVs) in C3NEW are moderately enhanced in strength. In the additional experiment
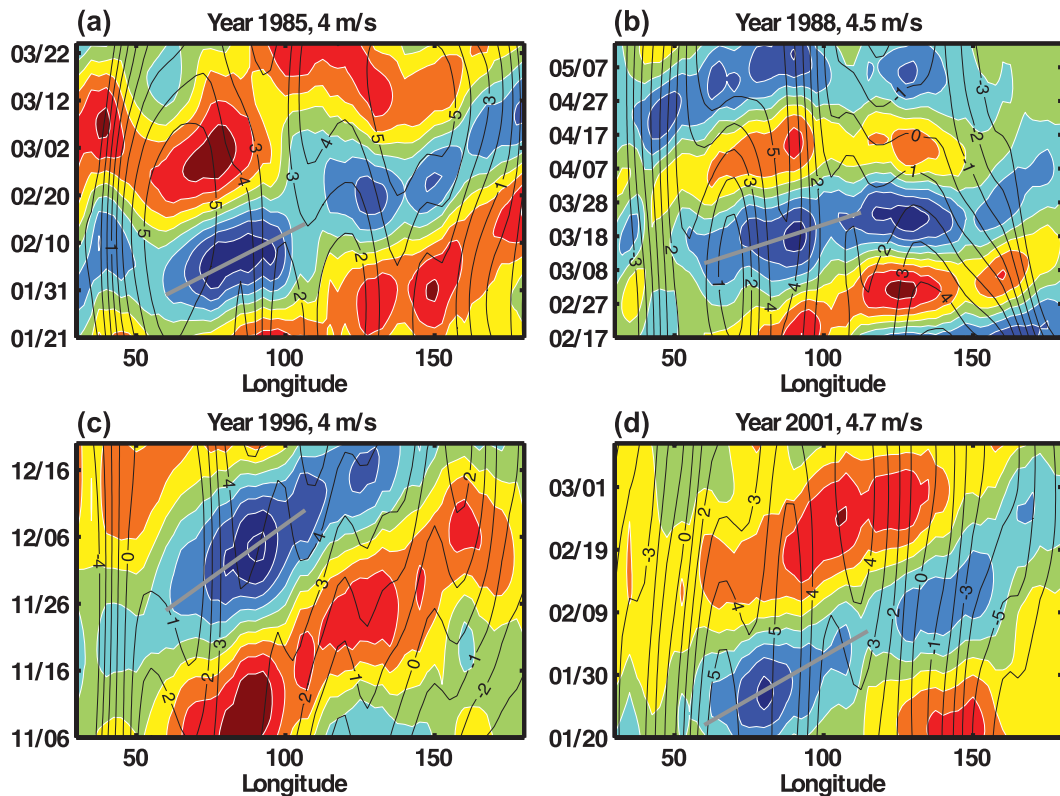
FIG. 15. Intraseasonal OLR anomalies from NOAA satellite (colors) and background zonal winds at 850 hPa from NCEP reanalysis. The estimated eastward propagation speed of each MJO event is marked in the title of each panel. It is also marked with a thick gray line in each panel. The contours of OLR anomalies are from -50 W m^{-2} (dark blue) to 50 W m^{-2} (dark red) with an interval of 10 W m^{-2}. The interval for the wind speed is 1 m s^{-1}.

C3DPA, it is also shown that inclusion of DPA helps to reinforce ISVs. With the inclusion of convective momentum transport (CMT), the low-level background zonal winds over the Indo-Pacific warm pool are reinforced and the easterly wind bias in this region is largely removed. The improved zonal winds tend to pace the eastward propagation of the enhanced ISVs, acting like a selective conveyor belt. In the experiment C3CMT, although the ISVs are not strong enough, the eastward propagation of ISVs is also discernable due to the improved westerly winds. Therefore, both modifications to the convection scheme in CCSM3 are helpful for the improvement of MJO simulations. The above conclusions are based on numerical experiments with one model. More tests with other models are necessary in the future. Moreover, inclusion of these two modifications to the convective parameterization alone may not guarantee a satisfactory MJO simulation. Although other GCMs may in principle include similar mechanisms to the CMT and dilution, the correct interaction among them and the rest of the model physics is also important. Different closure and triggering assumptions within the convection parameterization and the interaction with the rest of the

moist physics could have crucial impacts on tropical variability. For example, by the same token, the inclusion of CMT and DPA within the Unified Model (developed at the Met Office) has not been set to their optimal configuration for producing the most realistic results, but careful optimization should provide some improvement and understanding of the physical mechanisms involved.

The configuration of the atmospheric physical processes in C3OLD are nearly identical to CCSM3, which was the model submitted to the Intergovernmental Panel on Climate Change Assessment Report 4 (AR4). The major difference is in the dynamical core used. CCSM3 uses an Eulerian dynamical core that has been replaced by a finite volume representation (Lin and Rood 1996; Lin 2004) in all runs examined in this study. This has been shown to make no significant difference to the CCSM3 representation of the MJO. Even after the two modifications to the convective parameterization, the MJO simulation is still not completely satisfying. Currently, only a handful of models have anywhere near acceptable representation of the MJO [a superparameterized version of Community Atmosphere Model (CAM), which costs of the order 200 times to run than the standard CAM, and a version of the Hamburg

model ECHAM4 are the two of note]. The recently released version of the model CAM4/CCSM4 is vastly superior to CAM3/CCSM3 in many aspects of the mean simulation and variability (e.g., ENSO, rainfall frequency) due primarily to the inclusion of these two convection changes. Of course, the simulated MJOs need to be improved much more and the sources of the remaining deficiencies in this particular version of the model could include insufficient resolution (although T42 used in the current CCSM3 is still widely recognized as adequate resolution), poor surface coupling or continued poor representation or a lack of representation of certain processes. Naturally, all of these are ongoing research efforts in the CCSM community.

As articulated by the Working Group, the high degree of coherence is a very important feature of MJOs. By comparing CCSM3 simulations with and without DPA and CMT, we show that a better simulation of the background westerly winds in the tropical Indian Ocean and the western tropical Pacific Ocean facilitates a better organization of the simulated MJOs. The quadrature relation between the first two EOF modes is well captured in C3NEW, and the eastward propagation is similar to MJOs in nature as rendered by the reanalysis. With both the NCEP reanalysis and the model outputs, it is shown that the eastward propagation speed of the intraseasonal signals is tuned by the background zonal currents. The ISVs themselves, which can be regarded as stochastic perturbations to the background state (e.g., Newman et al. 2009), are not as well organized. Nevertheless, only the ISVs that are coherent with the background state can accumulate energy and propagate over a relatively long distance. Thus, the ISVs are selected (not just advected) and organized by the background state. Note that the background zonal winds are not independent of the mesoscale convection since CMT represents the feedback of mesoscale convection to the large-scale background state. Thus, the MJO speed is essentially the result of an interaction between mesoscale convection and the background circulation. With an aquaplanet model, Maloney et al. (2010) demonstrated that the synchronization between peak moistening and total westerly winds at 850 hPa determines the eastward propagation speed of the simulated MJOs, which was argued to also highlight the role of the coupling between convection and background winds in selecting the MJO speed. So far, most existing studies have focused on the one-way influence from the background state to the MJO simulation (such as Inness et al. 2003; Sperber et al. 2005; Zhang et al. 2006). Only a few studies discuss the influence of mesoscale convection on the background state, e.g., Ray et al. (2011). In our model experiments, convection can have feedbacks to the background state via CMT (Table 2) and lead to improvement in the simulation of the background state.

We believe that there should be consistency between a good simulation of MJOs and a good simulation of the background state. However, with current model configurations, it is not easy to make a robust conclusion on this. Thus, the influence of mesoscale convection on the simulation of background state needs to be addressed with specifically designed experiments in the future.

This conclusion confirms the importance of examining MJOs in a multiscale framework. A better simulation of the background state is helpful to achieve a better simulation of MJOs. In addition to the deep convection parameterization, regarded at present to be a major requirement for improving MJO simulations, this also calls for more attention to better representation and parameterization of the interactions between the large-scale circulation and the mesoscale ISVs. In particular, the hypothesis that the propagation speed of MJOs is closely related to the mean westerly winds is also consistent with the improvement of the eastward propagation of the simulated MJOs even when they are only approximately resolved in a model. The background states are also affected by changes in climate modes such as monsoons and ENSO. While that is consistent with the multiscale framework we are arguing for, the details of those interactions are not addressed here other than that they impact the background westerlies discussed here. Further details of the monsoon–ENSO–MJO interactions will be reported elsewhere.

REFERENCES

Agudelo, P. A., C. D. Hoyos, P. J. Webster, and J. A. Curry, 2009: Application of a serial extended forecast experiment using the ECMWF model to interpret the predictive skill of tropical intraseasonal variability. *Climate Dyn.,* **32,** 855–872.

Arakawa, A., and W. H. Schubert, 1974: Interaction of a cumulus cloud ensemble with the large-scale environment. Part I. *J. Atmos. Sci.,* **31,** 674–701.

Bechtold, P., J. P. Chaboureau, A. Beljaars, A. K. Betts, M. Kohler, M. Miller, and J. L. Redelsperger, 2004: The simulation of the diurnal cycle of convective precipitation over land in a global model. *Quart. J. Roy. Meteor. Soc.,* **130,** 3119–3137.

Benedict, J. J., and D. A. Randall, 2007: Observed characteristics of the MJO relative to maximum rainfall. *J. Atmos. Sci.,* **64,** 2332–2354.

Biello, J. A., and A. J. Majda, 2005: A new multiscale model for the Madden–Julian oscillation. *J. Atmos. Sci.,* **62,** 1694–1721.

Blade, I., and D. L. Hartmann, 1993: Tropical intraseasonal oscillations in a simple nonlinear model. *J. Atmos. Sci.,* **50,** 2922–2939.

Bretherton, C. S., and A. H. Sobel, 2002: A simple model of a convectively coupled Walker circulation using the weak temperature gradient approximation. *J. Climate,* **15,** 2907–2920.

——, and ——, 2003: The Gill model and the weak temperature gradient approximation. *J. Atmos. Sci.,* **60,** 451–460.

Chaboureau, J. P., F. Guichard, J. L. Redelsperger, and J. P. Lafore, 2004: The role of stability and moisture in the diurnal cycle of convection overland. *Quart. J. Roy. Meteor. Soc.,* **130,** 3105–3117.

Chao, W. C., and L. T. Deng, 1998: Tropical intraseasonal oscillation, super cloud clusters, and cumulus convection schemes. Part II: 3D aquaplanet simulations. *J. Atmos. Sci.,* **55,** 690–709.

——, and B. D. Chen, 2001: The role of surface friction in tropical intraseasonal oscillation. *Mon. Wea. Rev.,* **129,** 896–904.

CLIVAR Madden–Julian Oscillation Working Group, 2009: MJO simulation diagnostics. *J. Climate,* **22,** 3006–3030.

Collins, W. D., and Coauthors, 2006a: The formulation and atmospheric simulation of the Community Atmosphere Model version 3 (CAM3). *J. Climate,* **19,** 2144–2161.

——, and Coauthors, 2006b: The Community Climate System Model version 3 (CCSM3). *J. Climate,* **19,** 2122–2143.

Emanuel, K. A., 1987: An air–sea interaction model of intraseasonal oscillations in the tropics. *J. Atmos. Sci.,* **44,** 2324–2340.

——, J. D. Neelin, and C. S. Bretherton, 1994: On large-scale circulations in convecting atmospheres. *Quart. J. Roy. Meteor. Soc.,* **120,** 1111–1143.

Hendon, H. H., and B. Liebmann, 1994: Organization of convection within the Madden-Julian oscillation. *J. Geophys. Res.,* **99,** 8073–8083.

Hu, Q., and D. A. Randall, 1995: Low-frequency oscillations in radiative convective systems. Part II: An idealized model. *J. Atmos. Sci.,* **52,** 478–490.

Inness, P. M., and J. M. Slingo, 2003: Simulation of the Madden–Julian oscillation in a coupled general circulation model. Part I: Comparison with observations and an atmosphere-only GCM. *J. Climate,* **16,** 345–364.

——, ——, E. Guilyardi, and J. Cole, 2003: Simulation of the Madden–Julian oscillation in a coupled general circulation model. Part II: The role of the basic state. *J. Climate,* **16,** 365–382.

Johnson, R. H., T. M. Rickenbach, S. A. Rutledge, P. E. Ciesielski, and W. H. Schubert, 1999: Trimodal characteristics of tropical convection. *J. Climate,* **12,** 2397–2418.

Jones, C., 2009: A homogeneous stochastic model of the Madden–Julian oscillation. *J. Climate,* **22,** 3270–3288.

Kalnay, E., and Coauthors, 1996: The NCEP/NCAR 40-Year Reanalysis Project. *Bull. Amer. Meteor. Soc.,* **77,** 437–471.

Kemball-Cook, S. R., and B. C. Weare, 2001: The onset of convection in the Madden–Julian oscillation. *J. Climate,* **14,** 780–793.

Kershaw, R., and D. Gregory, 1997: Parametrization of momentum transport by convection. 1. Theory and cloud modelling results. *Quart. J. Roy. Meteor. Soc.,* **123,** 1133–1151.

Kim, D., and Coauthors, 2009: Application of MJO simulation diagnostics to climate models. *J. Climate,* **22,** 6413–6436.

Kuo, H.-L., 1974: Further studies of the parameterization of the influence of cumulus convection on large-scale flow. *J. Atmos. Sci.,* **31,** 1232–1240.

Lau, K. M., and L. Peng, 1987: Origin of low-frequency (intraseasonal) oscillations in the tropical atmosphere. Part I: Basic theory. *J. Atmos. Sci.,* **44,** 950–972.

Liebmann, B., and C. A. Smith, 1996: Description of a complete (interpolated) outgoing longwave radiation dataset. *Bull. Amer. Meteor. Soc.,* **77,** 1275–1277.

Lin, J. L., M. H. Zhang, and B. Mapes, 2005: Zonal momentum budget of the Madden–Julian oscillation: The source and strength of equivalent linear damping. *J. Atmos. Sci.,* **62,** 2172–2188.

——, and Coauthors, 2006: Tropical intraseasonal variability in 14 IPCC AR4 climate models. Part I: Convective signals. *J. Climate,* **19,** 2665–2690.

——, M. I. Lee, D. Kim, I. S. Kang, and D. M. W. Frierson, 2008: The impacts of convective parameterization and moisture triggering on AGCM-simulated convectively coupled equatorial waves. *J. Climate,* **21,** 883–909.

Lin, S.-J., 2004: A vertically Lagrangian finite-volume dynamical core for global models. *Mon. Wea. Rev.,* **132,** 2293–2307.

——, and R. B. Rood, 1996: Multidimensional flux-form semi-Lagrangian transport schemes. *Mon. Wea. Rev.,* **124,** 2046–2070.

Madden, R. A., and P. R. Julian, 1971: Detection of a 40–50 day oscillation in zonal wind in tropical Pacific. *J. Atmos. Sci.,* **28,** 702–708.

——, and ——, 1972: Description of global-scale circulation cells in tropics with a 40–50 day period. *J. Atmos. Sci.,* **29,** 1109–1123.

——, and ——, 1994: Observations of the 40–50-day tropical oscillation—A review. *Mon. Wea. Rev.,* **122,** 814–837.

——, and ——, 2005: Historical perspective. *Intraseasonal Variability in the Atmosphere-Ocean Climate System,* W. K.-M. Lau and D. Waliser, Eds., Springer-Praxis, 1–16.

Majda, A. J., and S. N. Stechmann, 2009: A simple dynamical model with features of convective momentum transport. *J. Atmos. Sci.,* **66,** 373–392.

Maloney, E. D., 2002: An intraseasonal oscillation composite life cycle in the NCAR CCM3.6 with modified convection. *J. Climate,* **15,** 964–982.

——, and D. L. Hartmann, 2001a: The sensitivity of intraseasonal variability in the NCAR CCM3 to changes in convective parameterization. *J. Climate,* **14,** 2015–2034.

——, and ——, 2001b: The Madden–Julian oscillation, barotropic dynamics, and North Pacific tropical cyclone formation. Part I: Observations. *J. Atmos. Sci.,* **58,** 2545–2558.

——, A. H. Sobel, and W. M. Hannah, 2010: Intraseasonal variability in an aquaplanet general circulation model. *J. Adv. Model. Earth Syst.,* **2,** doi:10.3894/JAMES.2010.2.5.

Manabe, S., J. Smagorinsky, and R. F. Strickler, 1965: Simulated climatology of a general circulation model with a hydrological cycle. *Mon. Wea. Rev.,* **93,** 769–798.

Moskowitz, B. M., and C. S. Bretherton, 2000: An analysis of frictional feedback on a moist equatorial Kelvin mode. *J. Atmos. Sci.,* **57,** 2188–2206.

Neale, R. B., J. H. Richter, and M. Jochum, 2008: The impact of convection on ENSO: From a delayed oscillator to a series of events. *J. Climate,* **21,** 5904–5924.

Neelin, J. D., I. M. Held, and K. H. Cook, 1987: Evaporation–wind feedback and low-frequency variability in the tropical atmosphere. *J. Atmos. Sci.,* **44,** 2341–2348.

Newman, M., P. D. Sardeshmukh, and C. Penland, 2009: How important is air–sea coupling in ENSO and MJO evolution? *J. Climate,* **22,** 2958–2977.

Pedlosky, J., 2003: *Waves in the Ocean and Atmosphere: Introduction to Wave Dynamics.* Springer, 260 pp.

Ray, P., and C. D. Zhang, 2010: A case study of the mechanics of extratropical influence on the initiation of the Madden–Julian oscillation. *J. Atmos. Sci.,* **67,** 515–528.

——, ——, M. W. Moncrieff, J. Dudhia, J. M. Caron, L. R. Leung, and C. Bruyere, 2011: Role of the atmospheric mean state on the initiation of the MJO in a tropical channel model. *Climate Dyn.,* **36,** 161–184.

Raymond, D. J., and A. M. Blyth, 1986: A stochastic mixing model for nonprecipitating cumulus clouds. *J. Atmos. Sci.,* **43,** 2708–2718.

——, and ——, 1992: Extension of the stochastic mixing model to cumulonimbus clouds. *J. Atmos. Sci.,* **49,** 1968–1983.

Richter, J. H., and P. J. Rasch, 2008: Effects of convective momentum transport on the atmospheric circulation in the community atmosphere model, version 3. *J. Climate,* **21,** 1487–1499.

Salby, M. L., R. R. Garcia, and H. H. Hendon, 1994: Planetary-scale circulations in the presence of climatological and wave-induced heating. *J. Atmos. Sci.,* **51,** 2344–2367.

Sardeshmukh, P. D., and P. Sura, 2007: Multiscale impacts of variable heating in climate. *J. Climate,* **20,** 5677–5695.

Slingo, J. M., and Coauthors, 1996: Intraseasonal oscillations in 15 atmospheric general circulation models: Results from an AMIP diagnostic subproject. *Climate Dyn.,* **12,** 325–357.

——, D. P. Rowell, K. R. Sperber, and E. Nortley, 1999: On the predictability of the interannual behaviour of the Madden–Julian oscillation and its relationship with El Nino. *Quart. J. Roy. Meteor. Soc.,* **125,** 583–609.

Sobel, A. H., J. Nilsson, and L. M. Polvani, 2001: The weak temperature gradient approximation and balanced tropical moisture waves. *J. Atmos. Sci.,* **58,** 3650–3665.

——, E. D. Maloney, G. Bellon, and D. M. Frierson, 2008: The role of surface heat fluxes in tropical intraseasonal oscillations. *Nat. Geosci.,* **1,** 653–657.

——, ——, ——, and ——, 2010: Surface fluxes and tropical intraseasonal variability: A reassessment. *J. Adv. Model. Earth Syst.,* **2,** doi:10.3894/JAMES.2010.2.2.

Sperber, K. R., and D. E. Waliser, 2008: New approaches to understanding, simulating, and forecasting the Madden–Julian oscillation. *Bull. Amer. Meteor. Soc.,* **89,** 1917–1920.

——, J. M. Slingo, P. M. Inness, and W. K. M. Lau, 1997: On the maintenance and initiation of the intraseasonal oscillation in the NCEP/NCAR reanalysis and in the GLA and UKMO AMIP simulations. *Climate Dyn.,* **13,** 769–795.

——, S. Gualdi, S. Legutke, and V. Gayler, 2005: The Madden–Julian oscillation in ECHAM4 coupled and uncoupled general circulation models. *Climate Dyn.,* **25,** 117–140.

Sugiyama, M., 2009: The moisture mode in the quasi-equilibrium tropical circulation model. Part I: Analysis based on the weak temperature gradient approximation. *J. Atmos. Sci.,* **66,** 1507–1523.

Sui, C. H., and K. M. Lau, 1989: Origin of low-frequency (intraseasonal) oscillations in the tropical atmosphere. Part II:

Structure and propagation of mobile wave-CISK modes and their modification by lower boundary forcings. *J. Atmos. Sci.,* **46,** 37–56.

Tian, B. J., D. E. Waliser, E. J. Fetzer, B. H. Lambrigtsen, Y. L. Yung, and B. Wang, 2006: Vertical moist thermodynamic structure and spatial-temporal evolution of the MJO in AIRS observations. *J. Atmos. Sci.,* **63,** 2462–2485.

——, ——, ——, and Y. L. Yung, 2010: Vertical moist thermodynamic structure of the Madden–Julian oscillation in atmospheric infrared sounder retrievals: An update and a comparison to ECMWF Interim Re-Analysis. *Mon. Wea. Rev.,* **138,** 4576–4582.

Tung, W. W., and M. Yanai, 2002: Convective momentum transport observed during the TOGA COARE IOP. Part I: General features. *J. Atmos. Sci.,* **59,** 1857–1871.

Waliser, D. E., K. M. Lau, and J. H. Kim, 1999: The influence of coupled sea surface temperatures on the Madden–Julian oscillation: A model perturbation experiment. *J. Atmos. Sci.,* **56,** 333–358.

Wang, B., 2005: Theory. *Intraseasonal Variability in the Atmosphere–Ocean Climate System,* W. K.-M. Lau and D. Waliser, Eds., Springer-Praxis, 307–360.

——, and H. Rui, 1990: Synoptic climatology of transient tropical intraseasonal convection anomalies—1975–1985. *Meteor. Atmos. Phys.,* **44,** 43–61.

Wang, W. Q., and M. E. Schlesinger, 1999: The dependence on convection parameterization of the tropical intraseasonal oscillation simulated by the UIUC 11-layer atmospheric GCM. *J. Climate,* **12,** 1423–1457.

Webster, P. J., and R. Lukas, 1992: TOGA-COARE: The coupled ocean–atmosphere response experiment. *Bull. Amer. Meteor. Soc.,* **73,** 1377–1416.

Wheeler, M. C., and G. N. Kiladis, 1999: Convectively coupled equatorial waves: Analysis of clouds and temperature in the wavenumber–frequency domain. *J. Atmos. Sci.,* **56,** 374–399.

——, and H. H. Hendon, 2004: An all-season real-time multivariate MJO index: Development of an index for monitoring and prediction. *Mon. Wea. Rev.,* **132,** 1917–1932.

Woolnough, S. J., J. M. Slingo, and B. J. Hoskins, 2001: The organization of tropical convection by intraseasonal sea surface temperature anomalies. *Quart. J. Roy. Meteor. Soc.,* **127,** 887–907.

Zhang, C. D., 2005: Madden–Julian oscillation. *Rev. Geophys.,* **43,** RG2003, doi:10.1029/2004RG000158.

——, and M. Dong, 2004: Seasonality in the Madden–Julian oscillation. *J. Climate,* **17,** 3169–3180.

——, ——, S. Gualdi, H. H. Hendon, E. D. Maloney, A. Marshall, K. R. Sperber, and W. Q. Wang, 2006: Simulations of the Madden–Julian oscillation in four pairs of coupled and uncoupled global models. *Climate Dyn.,* **27,** 573–592.

Zhang, G. J., and N. A. McFarlane, 1995: Sensitivity of climate simulations to the parameterization of cumulus convection in the Canadian Climate Center general circulation model. *Atmos.–Ocean,* **33,** 407–446.

——, and M. Q. Mu, 2005: Simulation of the Madden–Julian oscillation in the NCAR CCM3 using a revised Zhang–McFarlane convection parameterization scheme. *J. Climate,* **18,** 4046–4064.

Zhu, H. Y., H. Hendon, and C. Jakob, 2009: Convection in a parameterized and superparameterized model and its role in the representation of the MJO. *J. Atmos. Sci.,* **66,** 2796–2811.